Regional Crustal Imaging by Inversion of Multi-mode Rayleigh Wave Dispersion Curves Measured from Seismic Noise: Application to the Basque-Cantabrian Zone (N Spain)

A. Olivar-Castaño[1], M. Pilz[2], D. Pedreira[1], J. A. Pulgar[1], A. Díaz-González[1], J. M. González-Cortina[1]

[1]Department of Geology, University of Oviedo, C/Jesús Arias de Velasco S/N, 33005, Oviedo, Spain
[2]Helmholtz Centre Potsdam, GFZ German Research Centre for Geosciences, Telegrafenberg, 14473, Potsdam, Germany

Key Points:

- We present a complete inversion scheme for seismic-noise tomography that accounts for the contribution of higher modes of Rayleigh waves to the observed dispersion.
- We apply our proposed inversion scheme to data acquired by a dense seismic network deployed in the Basque–Cantabrian Zone.
- The final result is a 3D shear-wave velocity model of the crustal structure that significantly extends the area for which detailed information is available in the region.

Corresponding author: A. Olivar-Castaño, `olivar@geol.uniovi.es`

Abstract

Seismic-noise tomography is routinely applied for imaging geological structures at different spatial scales. The frequently used time-domain approach presents two limitations. First, extracting surface-wave group velocities from time-domain cross-correlations requires interstation distances of at least three wavelengths, which may be problematic when working at local or regional scales. Second, the presence of higher modes of surface waves in the cross-correlation functions is often disregarded, which may cause loss of valuable information about the shear-wave velocity structure. In this work, we present a complete inversion scheme that avoids these limitations, and use it to obtain a 3D shear-wave velocity model of the Basque–Cantabrian Zone (N Spain), a structurally complex area affected by multiple tectonic events. The resulting model agrees with the existing geological and geophysical knowledge and significantly extends the area for which high-resolution information is available.

1 Introduction

Passive seismic-imaging techniques have become popular in recent years. Particularly, the so-called seismic-noise tomography methodology (e.g., Bensen et al., 2007; Shapiro & Campillo, 2004) has been used to produce images of the Earth's structure at a wide range of scales and resolutions. For example, Saygin and Kennett (2010) computed group velocity maps for Rayleigh waves between 5 and 12.5s for the whole Australian continent, and Lin et al. (2008) produced a set of both Rayleigh and Love phase-velocity maps for the western United States. At a regional scale, Macquet et al. (2014) obtained a shear-wave velocity model for the Pyrenees and the adjacent foreland basins; and at a much smaller scale, Pilz et al. (2012) studied the local subsoil structure using data from a small-sized array of stations.

Besides a few studies focusing on body wave tomography (e.g., Poli et al., 2012), most seismic-noise tomography applications used ambient-noise cross-correlations to collect measurements of surface-wave velocities. However, the methodology used to collect these measurements was varied. Some approaches estimated group velocities from the time-domain cross-correlations (e.g., Bensen et al., 2007), while others directly determined phase velocities from the cross-correlation spectrum (e.g., Prieto et al., 2009; Ekström et al., 2009). In the time-domain approach, the cross-correlation of the ambient-noise recordings from two receivers is considered to be an estimate of the Green's function between those receivers (e.g., Lobkis & Weaver, 2001; Shapiro & Campillo, 2004). A classic frequency–time analysis (FTAN, e.g., Levsin et al., 1989) is often applied to the estimated Green's function (e.g., Lin et al., 2007) in order to measure group velocities. The advantage of this approach is its simplicity and ease of implementation, while producing results in good agreement with known geological features (e.g., Yang et al., 2007). As a drawback, reliable group velocity measurements require an interstation distance of at least three wavelengths (Bensen et al., 2007), and although some works suggested that this constraint can be relaxed (Boschi et al., 2013; Luo et al., 2015), this could still act as a severe limitation when working at local or regional scales (e.g., Lin et al., 2008). Moreover, while group velocity can be directly computed from phase velocity, the opposite requires solving a differential equation (Bensen et al., 2007).

Another often overlooked issue in most ambient-noise tomography applications is the contribution of higher modes of surface-wave propagation to the observed velocities (Bonnefoy-Claudet et al., 2006). Several studies have shown that the energy of the higher modes is affected by both source distance and the shear-wave velocity structure (e.g., Park et al., 2000; Tokimatsu et al., 1992). For instance, the presence of a superficial low-velocity layer may cause the higher modes to dominate the wavefield at certain frequency ranges (Shapiro et al., 2001). Therefore, not accounting for the possibility of higher modes of propagation affecting the measured surface wave velocities might lead to less accurate

results (Park et al., 2000). In this study we overcome the limitations by combining the approaches of Parolai et al. (2005) and Ekström (2014). Parolai et al. (2005) proposed a non linear joint-inversion scheme which accounts for the possible influence of the higher modes in the measured phase velocities. In the forward modeling, the dispersion curves and medium-response functions (Harkrider & Anderson, 1966) for the fundamental and higher modes are computed and subsequently combined into the apparent phase velocity following the formulation developed by Tokimatsu et al. (1992). Ekström (2014) avoided the three-wavelength minimum interstation distance affecting group velocity measurements derived from the estimated Green's function by computing instead phase velocities from the frequency-domain cross-correlation using the spectral formulation derived by Aki (1957).

The relationship between the phase velocities of surface waves and the vertical shear-wave velocity structure is highly nonlinear. Therefore, many different shear-wave velocity models can produce a phase velocity curve that fits the observations. By accounting for the higher modes of propagation of Rayleigh waves, additional information is provided to the inversion algorithm, reducing the number of possible solutions. This is particularly important when imaging structurally complex areas (i.e., areas with a very heterogeneous crust). The Basque-Cantabrian Zone (BCZ) of the Pyrenean–Cantabrian mountain belt in North-Iberia (Figure 1) is such a complex area, as evidenced by studies showing the presence of intracrustal high-velocity bodies and Moho depths that vary sharply across the region (e.g., Pedreira et al., 2003, 2007; Díaz et al., 2012; Chevrot et al., 2014). With the aim of providing an highly-resolved 3D image of the shear-wave velocity structure across this area, we apply the previously described approach to data acquired in a dense seismic network deployed in the BCZ between 2014 and 2018, with interstation distances ranging from 7 to 415 km (Figure 2). We then compare the results with the existing geological and geophysical knowledge of the area and discuss the methodological and tectonic implications.

2 Geological Setting

The studied area (Figure 1) is centered in the BCZ of the Pyrenean-Cantabrian mountain belt. This zone, now incorporated into the orogen, was one of the most subsident basins of the large rifting domain that was formed in the Mesozoic between Iberia and Eurasia, in relation to the opening of the North Atlantic ocean and the Bay of Biscay (Roca et al., 2011; García-Mondejar et al., 1996; Rat, 1988). Subsidence rates were very high, with some estimations for the thickness of the sedimentary cover reaching 15 km or even higher values (Quintana et al., 2015). The stratigraphy and inner structure of the Basque–Cantabrian Basin are highly heterogeneous (e.g., Cámara, 1997; Rat, 1988), reflecting the complexity of the evolving tectonosedimentary processes. During the Permian and the Triassic, the eroded Variscan basement was discontinuously covered by deposits of continental and shallow-marine origin deposited in small basins that were narrower in the Permian than in the Triassic (López-Gómez et al., 2019). The Jurassic sediments consist of a widespread carbonate platform series (e.g., Aurell et al., 2003) that is replaced by terrigenous sedimentation at the end of the Jurassic with the initiation of the major rifting phase. This phase prevailed during the Early Cretaceous, when continental to shallow marine sedimentation took place in the elevated blocks coeval with deposition of marls, sandstones and siltstones in the throughs (e.g., Rat, 1988). The stage of maximum crustal extension took place in the Aptian-Albian, with the mantle and lower crust being exhumed to the base of the sedimentary pile in the eastern part of the basin (DeFelipe et al., 2017; Roca et al., 2011). The Late Cretaceous sedimentation is essentially composed of widespread turbiditic deposits in the large subsident basin, with episodic events of alkaline volcanism (Azambre & Rossy, 1976; Castañares et al., 2001) and continental to shallow-marine platform deposits in the edges of the basin. The eastern border of the basin was marked by the Pamplona Transfer Zone (or Pamplona Fault), a NNE–

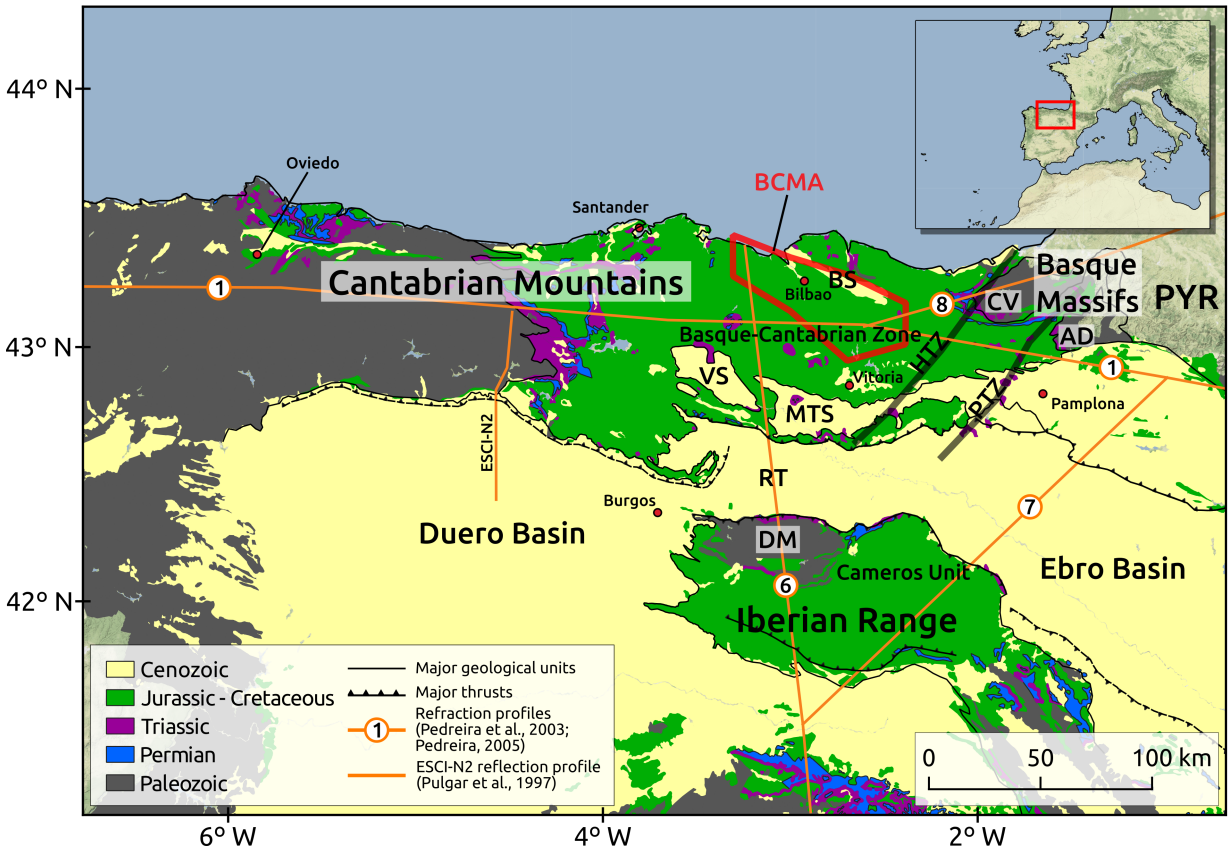

Figure 1. Geological map of the Basque–Cantabrian Zone and adjacent areas with the location of the seismic profiles used as constraints for the nonlinear inversion. AD: Alduides Massif; BCMA: outline of the highly-magnetized intra-crustal body responsible for the Basque-Country Magnetic Anomaly (BCMA; Pedreira et al., 2007); BS: Biscay Synclinorium; CV: Cinco-Villas Massif; DM: La Demanda Massif; HTZ: Hendaya Transfer Zone; MTS: Miranda-Treviño Syncline; PTZ: Pamplona Transfer Zone; PYR: Pyrenees; RT: Rioja Trough; VS: Villarcayo Syncline.

SSW deep structure that is not clearly visible at the surface but is outlined by the alignment of Triassic salt diapirs and concentration of seismic events (Larrasoaña et al., 2003; Ruiz et al., 2006). In the western border of the BCZ, the Mesozoic sediments are found unconformably overlying the Variscan basement.

During Cenozoic times, the convergence between the Iberian sub-plate and the European plate resulted in the inversion of the basin and its incorporation into the rising Pyrenean–Cantabrian orogen. The BCZ then became part of the Cantabrian Mountains, which constitute the western prolongation of the Pyrenees. Except for the northeastern corner of the BCZ, where north-vergent structures are found, the BCZ and the remaining Cantabrian Mountains to the west represent essentially the south-vergent wedge of the orogen, the north-vergent structures being located offshore. The Paleozoic basement located to the west of the basin, which was covered during the Cretaceous by a thin layer of Mesozoic platform deposits (still preserved in some patches,) was also uplifted in the Cenozoic, holding at present the higher elevations of the Cantabrian Mountains. This uplift took place in the Eocene–Oligocene, over a north-dipping crustal ramp along the southern orogenic front (Alonso et al., 1996; Fillon et al., 2016). In the BCZ, the frontal structure varies along strike, although it is mostly of a thin-skinned type, with the base-

ment involved in the deformation further north (e.g., Cámara, 2017; Carola et al., 2013). In fact, the Paleozoic basement crops out again around the northeastern border of the BCZ, forming the Basque Massifs (the largest of which are the Alduides and Cinco Villas massifs, Figure 1).

Toward the south of the studied area, the Rioja Trough (or La Bureba Corridor) accumulated up to 4 km of Cenozoic sediments from the erosion of the BCZ to the north and the Iberian Range to the south. This corridor connects the two large Cenozoic basins originated in the southern foreland of the Pyrenean–Cantabrian belt: the Duero and Ebro basins (Figure 1). The studied area also includes the northernmost part of the Iberian Range. During the Mesozoic, a continuous extensional basin existed in this area (the Cameros basin) with several depocenters and variable subsidence rates (Omodeo-Salé et al., 2015; Vidal, 2010). These Mesozoic rocks have been completely eroded in some areas after the Alpine uplift, like in La Demanda Massif, where the outcrops mainly show a thick succession of Paleozoic silicilastic rocks.

The geophysical observations of the deep Alpine structure of the BCZ are sparse. At the western border, the N–S seismic reflection profile ESCI-N2 (Pulgar et al., 1996) clearly shows the north-directed subduction of the Iberian crust (i.e., coherently with the Pyrenees). In 1997, a seismic refraction/wide angle reflection survey showed the lateral continuity of the crustal root: Moho depths along an E-W profile (Fig. 1) were found at 46–48 km from the Cantabrian Mountains to the Pyrenees, locally rising to ∼40 km beneath the western part of the BCZ (Pedreira et al., 2003). A high-velocity layer at mid-crustal depths along this profile was interpreted as the lower crust from the north Iberian (or Cantabrian) margin (i.e. the European domain) indented into the Iberian crust. The southernmost extent of this high-velocity layer varies from east to west, and is conditioned by the transfer structures of the basin that were also active as transfer structures during the orogenic event (Santander-Torrelavega, and Pamplona-Hendaya faults; Pedreira et al., 2003, 2007). This pattern of indentation was later refined by 3D gravity and magnetic modeling (Pedreira et al., 2007) and receiver functions analysis (Díaz et al., 2012). A smaller and shallower high-velocity body, identified in the E-W profile of the seismic refraction/wide-angle reflection at the eastern part of the BCZ, was interpreted as a segment of the mafic lower crust of the European domain thrusted toward the north. This body was considered by Pedreira et al. (2007) as the cause for the Basque Country Magnetic Anomaly (BCMA), the strongest aeromagnetic anomaly of the Spanish mainland (Aller & Zeyen, 1996; Ardizone et al., 1989). The outline of the strongly magnetized part of this body, projected onto the surface, is depicted in Figure 1. In recent years, several tomographic studies covering the BCZ have been published (Macquet et al., 2014; Palomeras et al., 2017; Silveira et al., 2013; Villaseñor et al., 2007). However, all of these works focus on a much larger scale and offer little detail on the local structure of the BCZ.

3 Data Collection and Preprocessing

The seismic data used in this study comes from the temporary MISTERIOS (Díaz & Pulgar, 2015) and SISCAN networks, deployed in the BCZ and adjacent areas (Figure 2) during the years 2014–2018. All stations were equipped with three-component broadband seismometers, each recording at a rate of 100 samples per second. Two different combinations of datalogger–seismometer were used, all made by Nanometrics: Centaur and Compact Posthole, or Taurus and Trillium 120P. The number and positions of the stations varied during the life of the networks, and these changes can be grouped in three different phases:

1. 2014–2016: Initial deployment of the seismic network. Twenty-nine broadband stations are installed across the BCZ (blue triangles and red squares in Figure 2).
2. 2016–2017: The stations installed during the first phase remain operational. Deployment of 14 stations at the eastern edge of the BCZ (green circles in Figure 2).

3. 2017–2018: Uninstallation of the stations located in the eastern edge of the BCZ (green circles in Figure 2), and deployment of new stations in the periphery of the study area (yellow rhombuses in Figure 2). Several stations of the initial deployment are also uninstalled (red squares in Figure 2).

Data preprocessing consists of several steps. First, the instrumental responses were removed from the vertical components of the continuous ambient noise recordings. Then, a low-pass filter with 1-Hz corner frequency was applied to prevent aliasing, after which the data were decimated to two samples per second. Next, the records were sliced into 2-h windows and normalized following the time-frequency normalization procedure described in Ekström et al. (2009). In this procedure a series of overlapping 1-mHz-wide filters are used to obtain nearly monochromatic signals. These signals are then divided by their amplitude envelopes and summed back together to form the normalized signal. In the last step, a 5% cosine taper was applied to the normalized vertical records before transforming them into the frequency domain.

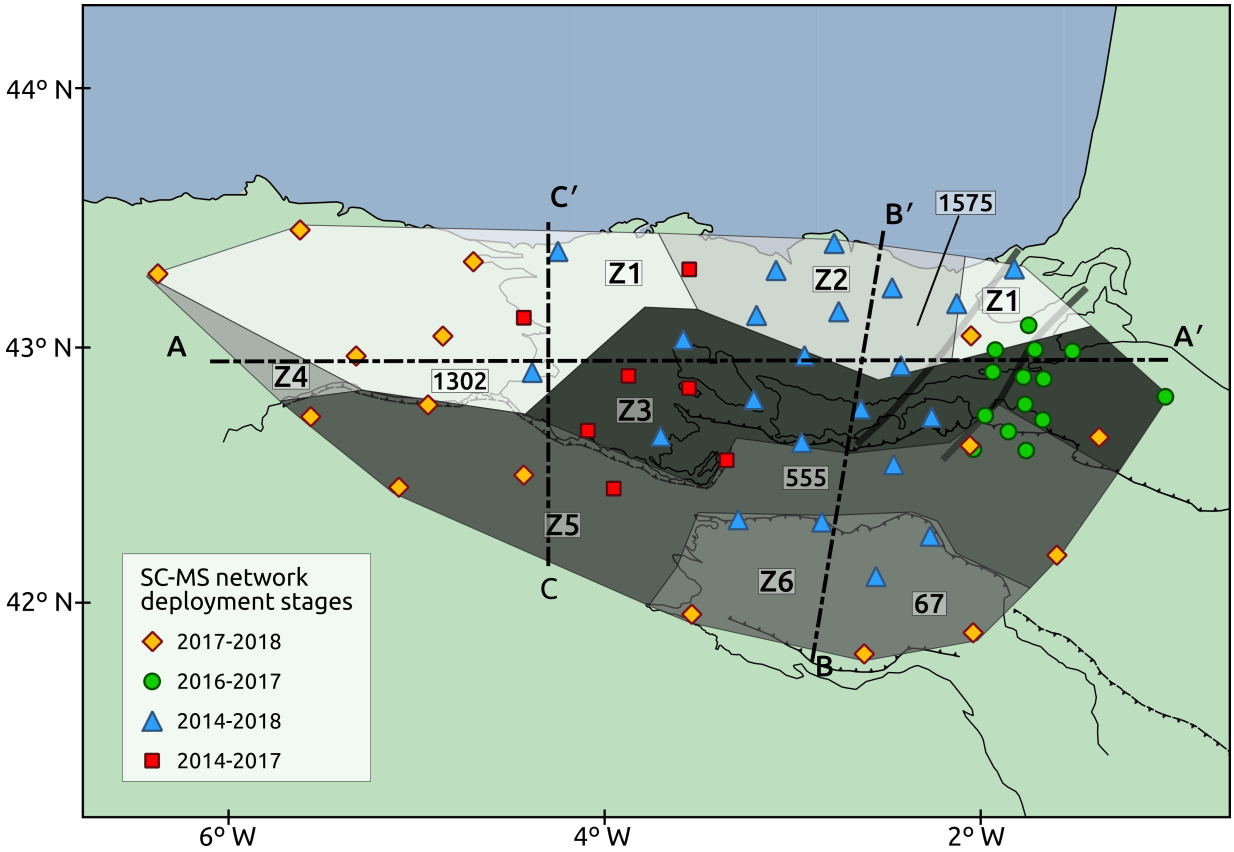

Figure 2. Depiction of the SISCAN (SC) and MISTERIOS (MS) network stations over the deployment period (early 2014 to late 2018, see legend). Areas in grayscale (labeled Z1 to Z6) show the geographical extent of the initial models used in the nonlinear inversion, while their parameters and constraints are shown in Table 1. The 1D shear-wave velocity models obtained for nodes 67, 555, 1302 and 1575 (white dots) are shown in Figure 7. Black dotted lines show the position of cross sections AA′, BB′, and CC′, shown in Figure 8

4 Methodology

Our inversion scheme involves four main steps: first, cross-correlation spectra of the vertical component are computed for all station pairs; second, phase velocities of Rayleigh waves are determined from the cross-spectra; third, a standard tomographic algorithm is applied to the measurements to obtain a set of phase-velocity maps; and fourth, a simulated annealing algorithm is used to determine the 1D shear-wave velocity at each node of a regular grid defined over the phase-velocity maps. In the following, we briefly describe the equations involved in the process. A detailed description of the methodology and mathematical background is available in the Supporting Information (Text S1 to S4).

The computation of the cross-correlation spectra is performed following Ekström (2014). Using the displacement spectra $u(\omega)$ for each pair of stations i, j and time window k the time-averaged cross-spectrum $\rho_{ij}^{S}(\omega)$ is:

$$\rho_{ij}^{S}(\omega) = \sum_{k=1}^{k=N} \frac{u_{ik}(\omega)u_{jk}^{*}(\omega)}{\sqrt{u_{ik}(\omega)u_{ik}^{*}(\omega)}\sqrt{u_{jk}(\omega)u_{jk}^{*}(\omega)}} \ , \tag{1}$$

where N is the total number of time windows, and the star * indicates the complex conjugate. The shape of $\rho_{ij}^{S}(\omega)$ is related to a first-kind Bessel function through the phase velocity $c(\omega)$ and receiver separation r (Aki, 1957; Ekström, 2014):

$$\rho_{ij}^{S}(\omega) = AJ_0\left(\frac{\omega}{c(\omega)}r\right) \ , \tag{2}$$

where A is an amplitude factor introduced in order to account for attenuation and normalization errors in the cross spectrum (Menke & Jin, 2015).

In order to determine the phase velocities using equation (2), we adopt the two-step procedure proposed by Menke and Jin (2015). First, we find initial estimates for the phase velocity $\mathbf{c}(\omega)$ and amplitude factor A through a standard grid search (e.g., Prieto et al., 2009). Although the solution obtained from the grid search will be the one which minimizes the error, the phase-velocity curve may contain physically implausible features (i.e., "kinks" or unrealistic jumps), which can influence the results. To avoid this, Menke and Jin (2015) proposed to use instead a linear fit to the initial estimate. However, we find that a custom exponential function can more realistically mimic the behavior of surface wave dispersion, as the rate of change of dispersion curves generally increases with increasing period (e.g., Tang et al., 2010; Pilz et al., 2017):

$$c(\omega) = d\ \tanh^{-1}(e\,\omega) + \frac{f}{\sqrt{\omega}} \ , \tag{3}$$

where d, e and f are constant parameters that can be easily found through trial and error (i.e. any Monte-Carlo method). The second step in the determination of phase velocities is to refine the initial estimates by iterative least-squares regression. For this, the relationship described by equation (2) is linearized around a certain estimate solution $\mathbf{m}^{(p)} = [\mathbf{c}(\omega)^p, A^p]$, leading to the linear equation (Menke & Jin, 2015):

$$\mathbf{G}\Delta\mathbf{m} = \Delta\boldsymbol{\rho} \ , \tag{4}$$

where $\mathbf{G}$ is the data kernel, $\Delta\mathbf{m} = \mathbf{m} - \mathbf{m}^{(p)}$ is the difference between the refined solution and the estimate, and $\Delta\boldsymbol{\rho} = \boldsymbol{\rho}^{obs} - \boldsymbol{\rho}^{pre}(\mathbf{m}^{(p)})$ is the difference between the observed cross-spectrum and the one predicted using the estimate $\mathbf{m}^{(p)}$ and equation (2). Starting with the initial estimate obtained in the previous step as $\mathbf{m}^{(p)}$, equation (4) is iteratively solved until $\Delta\boldsymbol{\rho}$ is sufficiently small (i.e. less than 1 per cent of $\boldsymbol{\rho}^{obs}$). As an example, Figure 3 shows the results of the waveform-fitting procedure for station pair MS02–SC16, with the top and bottom graphs featuring the fitted cross-spectrum and the corresponding phase-velocity curve, respectively. This computation was performed

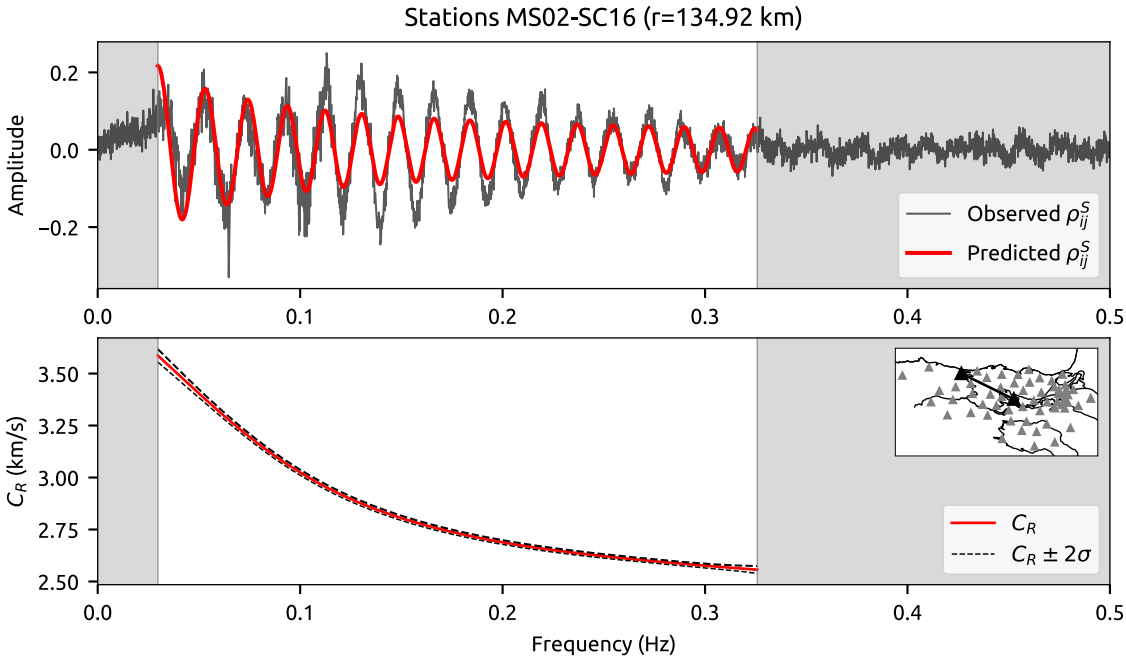

Figure 3. Result of the waveform fitting procedure for station pair MS02-SC16, separated by 134.92 km. (top) Stacked cross-spectrum p_{ij}^S (black line) and best-fitting Bessel function (red line). Grey areas represent parts of the cross-spectrum with poor SNR that can not be fitted correctly. (bottom) Rayleigh wave phase-velocity curve computed using the best-fitting Bessel function (red line) and 95% confidence interval (black lines). The small plot on the top right corner shows the position of the station pair in the network.

for all available station pairs in the frequency range in which the cross-spectrum has an acceptable signal-to-noise ratio (e.g., Figure 3, top graph). For our dataset, the total number of cross-spectra that pass this criterion is highest for periods ranging from 4 to 31 s, and decreases steadily for longer periods (Figure 4). Therefore, in the next steps, we focused on the period range from 4 to 40 s, as this allowed us to maximize our investigation depth (i.e., using the longest wavelengths possible) while maintaning a sufficient data coverage at all considered periods. Figure 5a shows schematically the waveform fitting process.

Once phase velocities have been determined for all station pairs, a set of phase velocity maps is built using the tomographic algorithm described by Barmin et al. (2001). In this approach, velocities across the study area are parametrized using a grid of regularly spaced nodes. We chose a spacing of 5 km between adjacent nodes, since our shortest interstation distance is approximately 7 km. Surface waves are treated as rays traveling along the great circle linking sources and receivers, and therefore the relationship between the data and model parameters can be expressed through the linear equation:

$$\mathbf{Gm} = \mathbf{d} \ , \tag{5}$$

where $\mathbf{G}$ is again the data kernel; the data vector $\mathbf{d}$ contains the travel-time perturbations between source and receiver; and the parameter vector $\mathbf{m}$ contains the slowness perturbations along the nodes, both of them relative to a reference model (i.e., a homogeneous velocity map). For any given period, we only include in equation (5) those source-receiver pairs that are separated by at least one wavelength, as we consider this to be

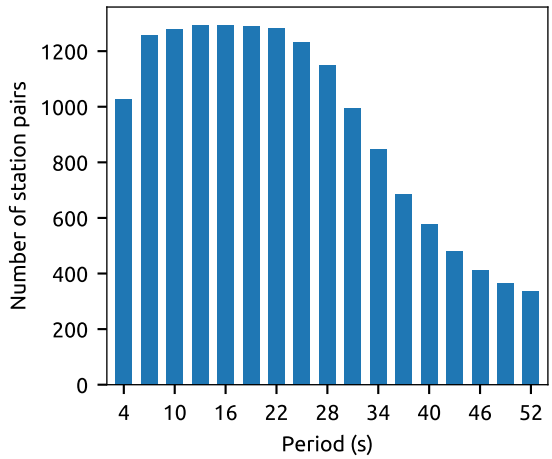

Figure 4. Histogram showing the available number of measurements (station pairs) as a function of the period that fulfill the SNR criterion.

the lower limit of our resolution. The vector $\mathbf{m}$ is estimated by minimization of the penalty function (Barmin et al., 2001; Goutorbe et al., 2015):

$$E(\mathbf{m}) = (\mathbf{Gm} - \mathbf{d})^T \mathbf{C}^{-1} (\mathbf{Gm} - \mathbf{d}) + \alpha^2 ||\mathbf{Fm}||^2 + \beta^2 ||\mathbf{Hm}||^2 \ . \tag{6}$$

The first term of the penalty function represents data misfit. The covariance matrix $\mathbf{C}$ is a diagonal matrix whose non-zero elements are the variances of the observed travel-times, which can be estimated from the variance of the phase-velocity curves. The second and third terms incorporate the regularization constraints for the inversion. The term $\alpha^2 ||\mathbf{Fm}||^2$ is a spatial smoothing condition, while the term $\beta^2 ||\mathbf{Hm}||^2$ penalizes deviations from the chosen reference model. Parameters α and β control the strength with which these conditions are applied. The spatial smoothing condition contains an additional spatial correlation parameter σ, while the sharpness of the weighting function $\mathbf{H}$ is controlled by a factor λ. The four regularization parameters α, β, σ, and λ are chosen through a trial-and-error process which involves visual inspection of the resulting phase-velocity maps (for an example, see Figure S2 in the Supporting Information). A good choice of parameters should yield maps that are smooth and free from artifacts, and small variations (less than 30%) of the parameters should not affect the results significantly (Barmin et al., 2001). Further details on how to choose appropiate regularization parameters can be found in the original work by Barmin et al. (2001) or Ritzwoller and Levshin (1998). The travel-time inversion is performed twice to detect and remove outliers from the dataset, as suggested by Barmin et al. (2001). On the first run, a large value for α is chosen so that the inversion is overdamped and yields a smooth tomographic map. Then, the observed travel times are compared with those predicted from the overdamped result. If a residuals is greater than two standard deviations, the corresponding measurement is discarded. This step discards between 3-5% of all measurements at any given period (for an example of the effects this has on the resulting phase velocity maps, see Figure S3 in the Supporting Information). The spatial resolution can be estimated by fitting a cone to each row of the resolution matrix $\mathbf{R}$, which can be computed as:

$$\mathbf{R} = (\mathbf{G}^T \mathbf{C}^{-1} \mathbf{G} + \mathbf{Q})^{-1} \mathbf{G}^T \mathbf{C}^{-1} \mathbf{G}. \tag{7}$$

where matrix $\mathbf{Q}$ includes the regularization constraints,

$$\mathbf{Q} = \alpha^2 \mathbf{F}^T \mathbf{F} + \beta^2 \mathbf{H}^T \mathbf{H}. \tag{8}$$

Finally, dispersion curves are compiled from the set of phase-velocity maps and inverted for the 1D shear-wave velocity structure by means of a simulated annealing algorithm (Kirkpatrick et al., 1983; Menke, 2012). Simulated annealing is a part random, part directed iterative minimization method controlled by two parameters: temperature (T), which decreases with each iteration, and misfit (E). The algorithm, shown schematically in Figure 5b, starts with a trial solution and randomly searches the model space for new solutions. New solutions are always accepted and replace the trial solution if the misfit E decreases; however, they can also be accepted even if E increases, with a probability $p(m)$ (Menke, 2012):

$$p(m) \propto \exp\left(\frac{-E(m)}{T}\right) . \tag{9}$$

Therefore, when T is large, new solutions are frequently accepted and a random search is conducted; however, this becomes less likely as iterations progress and T becomes smaller, with the search becoming increasingly directed. The selection of the cooling schedule (i.e., how T decreases with each passing iteration) is a complex issue (e.g., Ben-Ameur, 2004; Kirkpatrick, 1984); however, as a general rule, an acceptance ratio of 80% for new solutions is appropriate for the first few hundred iterations (Kirkpatrick, 1984). The misfit E is chosen as the squared misfit to the observed dispersion curve (Goutorbe et al., 2015):

$$E = \frac{1}{2}\sum_i \left[\frac{c_R^{\text{app}}(\omega_i) - c_R^{\text{obs}}(\omega_i)}{\sigma^{\text{obs}}(\omega_i)}\right]^2 , \tag{10}$$

where $c_R^{\text{app}}(\omega)$ is the theoretical dispersion curve resulting from the forward computation, and $\sigma^{\text{obs}}(\omega)$ is the standard deviation of the observed phase velocities at frequency ω. For the forward modeling, Rayleigh wave dispersion curves for the fundamental and higher modes are computed using the matrix propagator method (Haskell, 1953), in which the Earth is represented by a stack of layers overlying a homogeneous half-space. As the original method is prone to numerical instabilities (Schwab & Knopoff, 1970; Aki & Richards, 2002), we implement the orthonormalization scheme described by Wang (1999). Once computed, the fundamental- and higher-modes dispersion curves are combined together into the apparent dispersion curve $c_R^{\text{app}}(\omega)$, following Tokimatsu et al. (1992):

$$\cos\left(\frac{\omega D}{c_R^{app}(\omega)}\right)\sum_{m=0}^{M} A_{R_m}^2(\omega)c_{R_m}(\omega) = \sum_{m=0}^{M} A_{R_m}^2(\omega)c_{R_m}(\omega)\cos\left(\frac{\omega D}{c_{R_m}(\omega)}\right) , \tag{11}$$

where $c_{R_m}(\omega)$ and $A_{R_m}(\omega)$ are the dispersion curve and the medium-response function, respectively (e.g., Harkrider, 1964; Ben-Menahem & Singh, 2000; García-Jerez et al., 2016) associated with the m-th Rayleigh wave mode. The importance of the contribution of each mode to the apparent dispersion curve is mainly dependent on the medium response function $A_{R_m}(\omega)$, which is in turn dependent on the shear-wave velocity structure. Ohori et al. (2002) set D as the smallest inter-station distance in their array. In our approach, we set D as the distance between adjacent nodes of the grid used to obtain the phase-velocity maps.

The initial models and constraints used in the nonlinear inversion are detailed in Table 1. The study area was divided into six different regions considering the existing geological and geophysical knowledge (Figure 2). This internal subdivision represents a compromise between considering areas with broadly similar geological-geophysical characteristics and areas with similar shapes for the dispersion curves. We assigned an initial shear-wave velocity model to each region (Table 1) built from the results of the seismic refraction/wide angle reflection profiles displayed in Figure 1 (Pedreira et al., 2003; Pedreira, 2005). Zones 1 and 2 essentially correspond to regions where the crustal structure was deeply modified by the Alpine orogenic event, resulting in a significant crustal root and a velocity inversion created by the indentation of the European lower crust into the Iberian crust (Pedreira et al., 2003, 2007). The main difference between the two zones is that in Zone 2 a shallower high-velocity body was found centered at around 10 km depth

in seismic refraction/wide-angle reflection profiles (Pedreira et al., 2003; Pedreira, 2005), creating another velocity inversion. Pedreira et al. (2007) suggest that this body may correspond to the southern edge of the indenting European mafic lower crust that was thrusted to the north during the orogenic process, originating also the so called Basque-Country Magnetic Anomaly (Aller & Zeyen, 1996; Ardizone et al., 1989). The geographical extension of Zone 2, however, is larger than the inferred contour of this body, in order to check the robustness of the method when choosing whether to preserve the shallower inversion of the initial model or not. Zone 3 lies to the south of the southernmost extent of the indenting European lower crust (Pedreira et al., 2007) and, consequently, there is no intracrustal velocity inversion and the crustal thickness is significantly lower here. It also has lower velocities near the surface due to the presence of thick Cenozoic sediments. Zone 4 corresponds to marginal areas of the Pyrenean-Cantabrian mountain belt where the Alpine orogenic deformation did not affect in a significant way the older, 30 km thick, Variscan crust. Zone 5 is restricted to the Cenozoic foreland basins (Duero, Ebro and La Rioja trough), which were developed on top of an almost unthickened Variscan crust, and finally, Zone 6 corresponds to the Iberian range, with moderate crustal thickening.

5 Results

5.1 Rayleigh Wave Phase Velocity Maps

Phase-velocity maps at 5-, 8- and 14-s periods, along with their respective resolution maps and interstation paths are shown in Figure 6. As expected, at short periods the phase-velocity maps resemble the surface geology (Figure 1). The highest relative velocities are observed in areas where the Paleozoic basement crops out or is very near the surface: in the Cantabrian Mountains westwards of the BCZ, in the northeastern border if the BCZ, and in the Iberian Range (La Demanda massif and surrounding areas) to the south. Low velocities are concentrated in areas with thick Cenozoic sediments, either outcropping (La Rioja Trough, Duero and Ebro foreland basins, Villarcayo and Miranda-Treviño synclines; Figure 1) or preserved in the footwall of the southern frontal thrust of the Pyrenean-Cantabrian belt. These features persist with increasing period, as velocity contrasts become progressively smaller. At periods higher than 20 s, distinct features cannot be clearly observed, as the resolution becomes poorer due to the increasing wavelengths and the decreasing number of available interstation paths. Spatial resolution values are approximately 40 km on average at a period of 5 s, reaching down to 25 km in close proximity to some of the stations, and consistently increase with increasing period (e.g., the average resolution of ∼60 km at a period of 14 s; Figure 6). In general, the average phase velocity increases with increasing period; however, a sharp drop occurring at around 0.18 Hz can be observed in the Eastern Basque-Cantabrian Zone (e.g., node 1575: see phase velocity curve in Figure 7 and location in Figure 2).

5.2 Shear-Wave Velocity Model

The described nonlinear inversion was performed for a total of 2,136 locations, corresponding to a regular grid inside of the area of ray-path coverage (Figure 6), with a spacing of 5 km between adjacent nodes. The resulting 1D models were then linearly interpolated to create the 3D model of the study area. Shear-wave velocity models representative of different regions are shown in Figure 7. The higher mode contribution is subtler in areas where the V_S monotonically increases with depth, like in the Rioja Trough (Figure 7, node 555) and Iberian Range (Figure 7, node 67), and becomes more noticeable for the complex structures beneath the central Cantabrian Mountains (Figure 7, node 1302) and the Eastern Basque-Cantabrian Zone (Figure 7, node 1575).

E–W and N–S cross sections, as well as horizontal slices of the model at depths of 5, 10, and 22 km are presented in Figure 8. The major geological features represented

Table 1. Detailed description of the initial models (built from the seismic velocity-depth profiles of Pedreira et al. (2003); Pedreira (2005)) and the constraints used in the non-linear inversion for the different zones of the study area (the greyscale areas shown in Figure 2). The V_P/V_S ratio is fixed at 1.73. Layer parameters are enumerated from shallowest to deepest.

Zone	Z1	Z2	Z3	Z4	Z5	Z6
Layers	6	7	6	6	6	6
Layer thickness (km)	4.00, 7.00, 6.50, 8.50, 12.50, 11.50	3.00, 4.50, 4.00, 5.50, 9.50, 9.00, 13.00	5.00, 5.00, 5.00, 5.00, 10.00, 9.00	3.00, 3.00, 5.00, 5.00, 7.00, 7.00	4.00, 6.00, 5.00, 5.00, 9.00, 8.00	4.00, 6.00, 6.00, 7.00, 10.00, 7.00
V_P **(km/s)**	5.00, 5.80, 6.15, 7.00, 6.50, 6.95	4.80, 5.00, 6.90, 5.50, 7.20, 6.50, 6.95	4.75, 5.80, 6.20, 6.20, 6.30, 6.90	5.20, 5.40, 5.90, 6.15, 6.25, 6.70	4.50, 5.20, 5.85, 6.10, 6.20, 6.70	5.00, 5.90, 6.20, 6.20, 6.30, 6.75
Velocity inversions (depth range in km)	Allowed (20-40)	Allowed (8-40)	No	No	No	No
Depth to halfspace (range in km)	40-55	40-55	31-46	20-40	32-42	35-45
Halfspace V_P **range (km/s)**	7.90-8.50	7.90-8.50	7.90-8.50	7.70-8.30	7.70-8.30	7.70-8.30

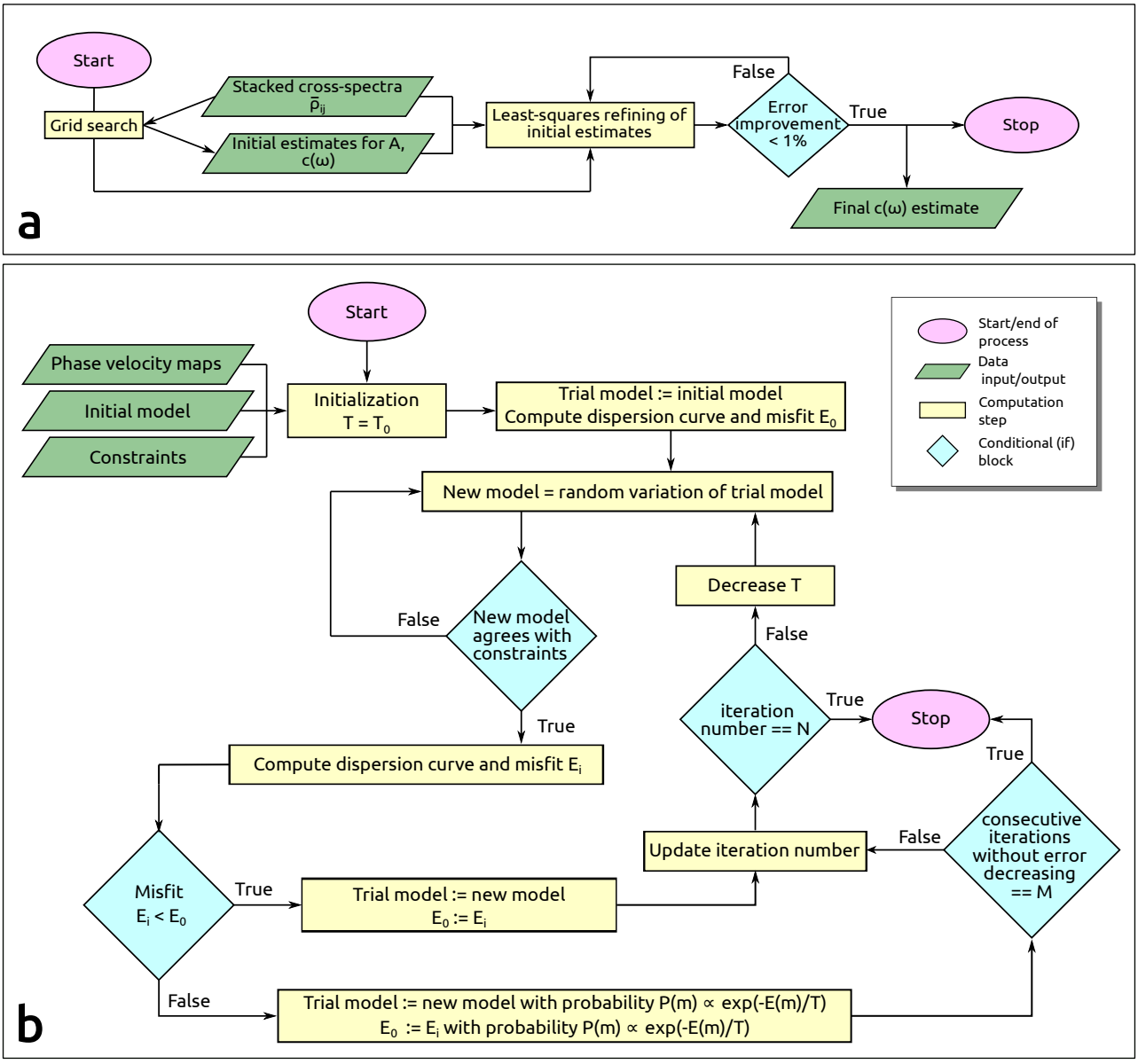

Figure 5. Flowchart describing the steps followed in (a) the waveform fitting procedure to measure Rayleigh wave phase velocities from the cross-spectra, and (b) the nonlinear inversion (simulated annealing) to find the best-fitting shear-wave velocity models.

in Figure 1 can be clearly seen at a depth of 5 km. The highest velocities at this depth, of ∼3.3 km/s, are found in the Paleozoic rocks of the Cantabrian Mountains to the northwest. Other Paleozoic massifs such as the Cinco-Villas to the northeast and La Demanda to the south of the study area show slightly lower velocities (ranging from 3.0 to 3.2 km/s). The Mesozoic materials of the BCZ have lower velocities in general (∼2.85 km/s), except at the northwestern end of the BCZ, which could be explained by a lower thickness of the sedimentary cover in that area, as imaged in the available seismic refraction profiles (Pedreira et al., 2003). The lowest relative-velocity anomalies (up to -10%) at this depth outline the slower Cenozoic materials in the southern BCZ (Villarcayo and Miranda-Treviño) and in the Ebro and Duero Basins.

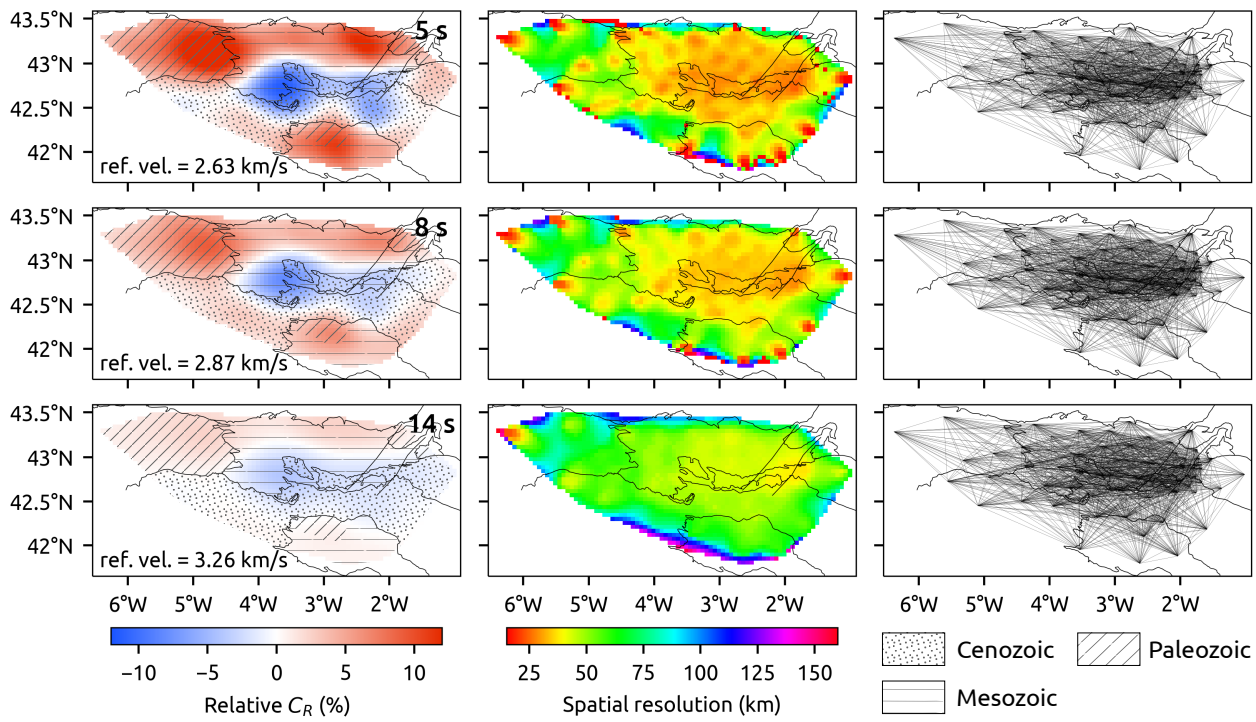

Figure 6. Maps showing the phase velocity of Rayleigh waves (denoted by c_R) (left column) for periods of 5s (top), 8s (middle) and 14s (bottom) with their resolution maps (middle column) and interstation paths (right column) used in the inversion. The "ref. vel." value on each map represents the reference velocity to which the velocity variations are given. The dotted and striped patterns in the phase velocity maps intend to show the locations of Cenozoic, Mesozoic and Paleozoic outcrops in a general manner.

At a depth of 10 km, the Ebro and Duero basins are outlined by a high relative-velocity anomaly that would corresponds to the Iberian upper crust. Low-velocity anomalies continue to be observed in the southern BCZ and the Cameros Unit, due to the higher thickness of the Mesozoic materials, and to the east of the PTZ, in the thick Cenozoic Jaca-Pamplona basin of the South-Pyrenean Zone. An interesting and well-defined high-velocity anomaly at this depth between the Bilbao area and the HTZ can be clearly seen in both cross-sections (Figure 8).

Starting at a depth of ∼17 km (cross section AA′, Figure 8), a W to E trending high-velocity feature begins to appear. This feature can be clearly seen in the horizontal slice at 22 km depth in Figure 8, extending from the Cantabrian Mountains in the west to the Basque Massifs in the northeast, and occupying roughly the northern half of the study area before progressively disappearing to the south (cross section BB′, Figure 8). This high-velocity layer, which extends down to 25–27 km, is interpreted as an indentation of the Cantabrian margin/European lower crust (e.g., Pedreira et al., 2003, 2007; Quintana et al., 2015).

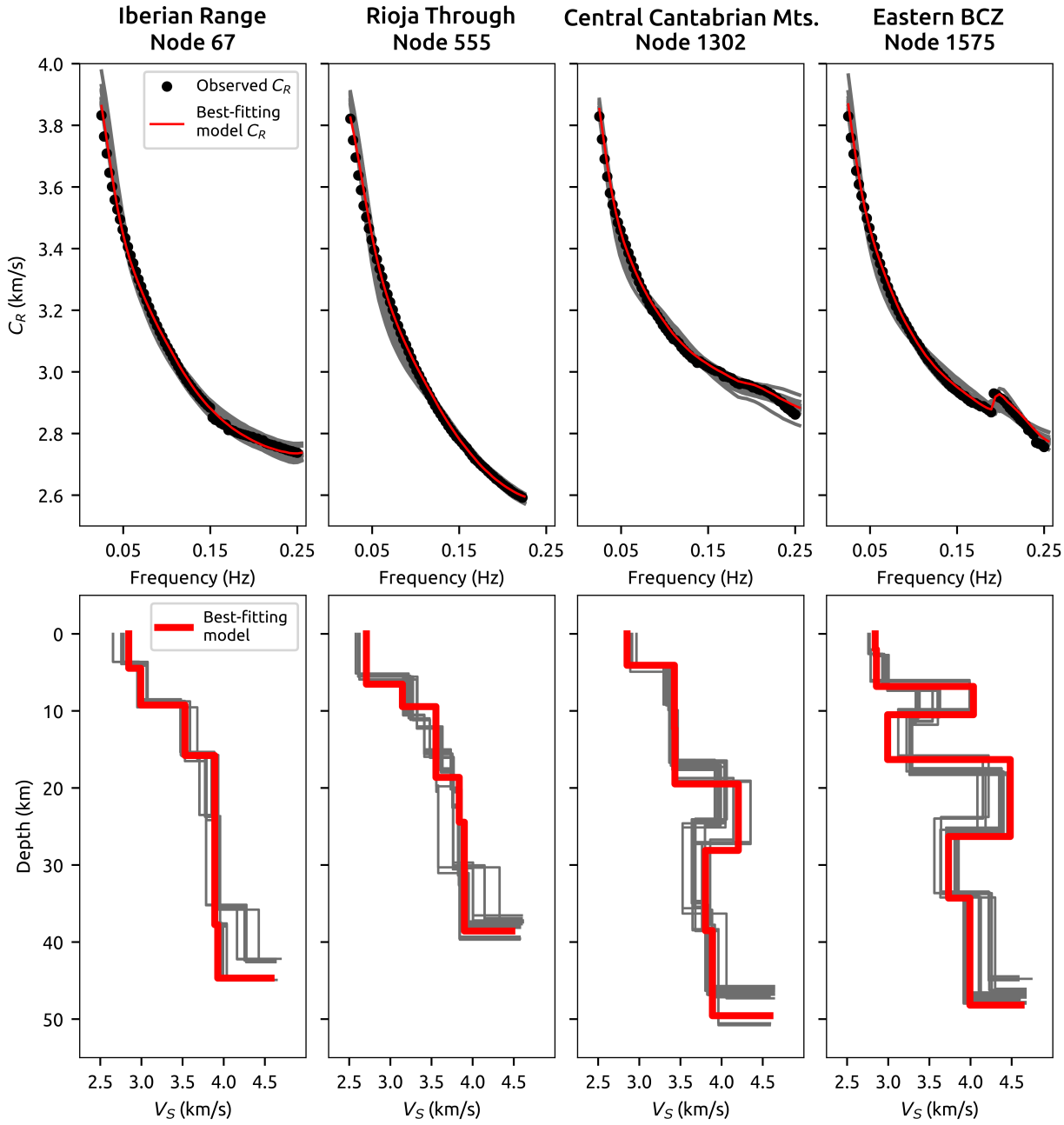

Figure 7. Selected inversion results representative of the different shapes of the dispersion curves observed in the study area (grid nodes 67, 555, 1302 and 1575, shown as white dots in Figure 2). (top) Best-fitting dispersion curve (red line) plotted against the values compiled from the phase velocity maps (black dots). The dispersion curves associated with the 10% best fitting models are shown as gray lines. (bottom) Best fitting shear-wave velocity models at each location (red line) and 10% best-fitting models (gray lines).

6 Discussion

The results presented in this study show for the first time a high-resolution shear-wave velocity model of the entire BCZ. Although Moho depths are the less constrained

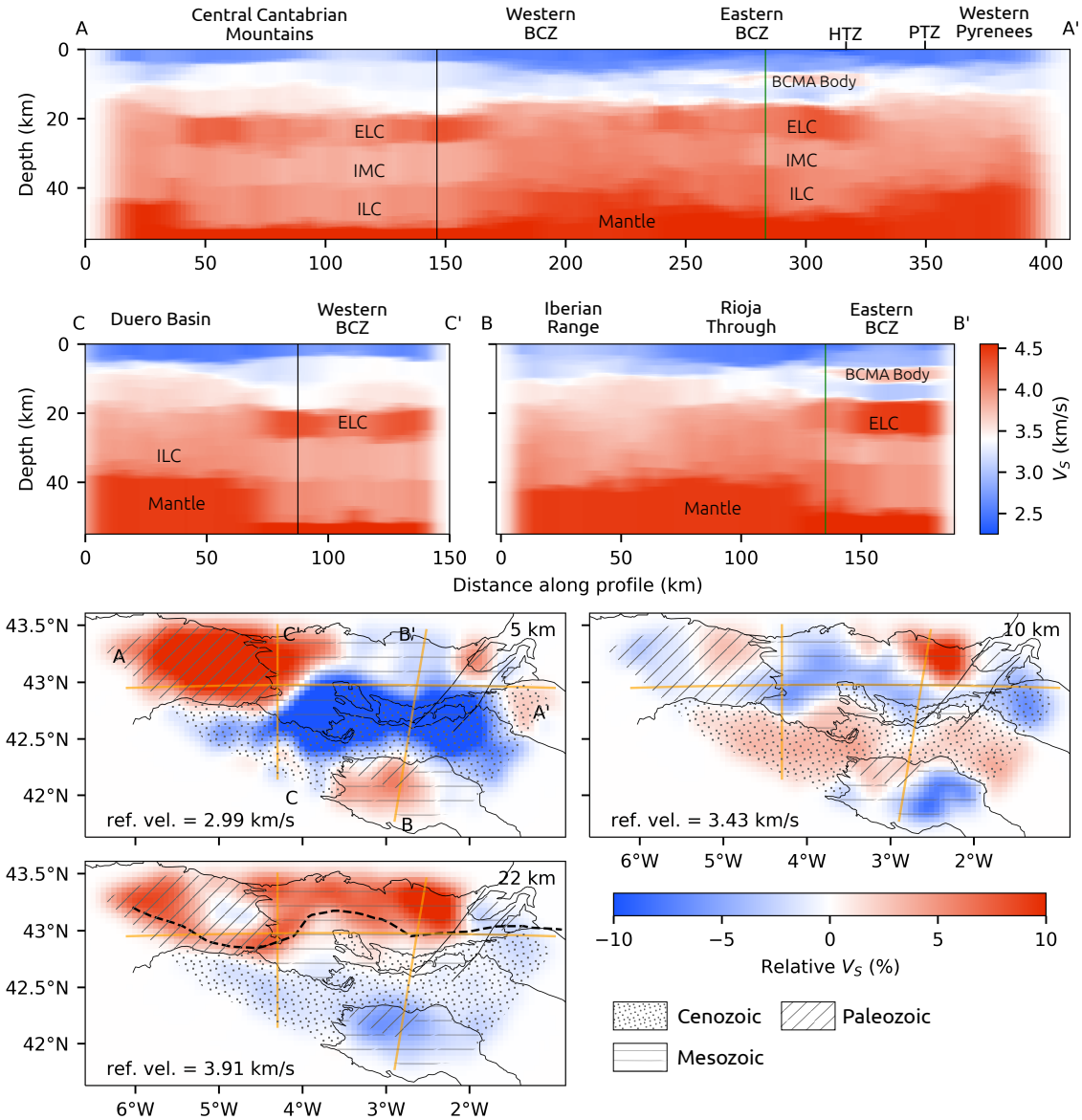

Figure 8. (top) Cross sections AA′ (W to E), BB′ (SSW to NNE), CC′ (S to N) showing absolute V_S velocities. The green and black vertical lines represent the intersection of profiles BB′ and CC′ with profile AA′, respectively. The interpretation of the different crustal layers is made according to Pedreira et al. (2003): BCMA body: intra-crustal body associated to the Basque-Country Magnetic Anomaly; ELC: European lower crust; ILC: Iberian lower crust; IMC: Iberian middle crust. (bottom) Horizontal slices from the shear-wave velocity model at depths of 5, 10 and 22 km showing the main features discussed in the text. The orange lines show the location of the cross-sections. The dotted and striped patterns intend to show the locations of Cenozoic, Mesozoic and Paleozoic outcrops in a general manner. The black dashed line in the 22 km plot (bottom left) indicates the southernmost position of the European lower crust according to the 3D gravity model by Pedreira et al. (2007).

feature of our model, we can still resolve a significant variation between the northern and southern zones of the study area (cross section CC′, Figure 8). In general, the crust in the northern part of the study area features a great thickness, with Moho depths ranging approximately from 50 to 45 km, rising slightly towards the east below the western BCZ (cross section AA′, Figure 8). Moho depths become much shallower to the south of the study area, reaching 38 km below the Rioja Trough (cross-section BB', Figure 8). These results differ from the Moho depths found by Palomeras et al. (2017), which reach 30 km in the BCZ, but they do agree well with the findings of Chevrot et al. (2014), who combined observations from receiver functions and seismic reflection/refraction profiles to create a map of crustal thicknesses that covers our study area. Their results feature Moho depths of up to 50, 40–44, and 38 km below the central Cantabrian Mountains, the BCZ, and the Basque Massifs, respectively.

Cross section AA′ shows the thickened crust in the northern part of the study area, featuring a high-velocity layer in the ∼17–25 km depth range which we interpret as the Cantabrian margin/European lower crust. The crustal thickening beneath the Cantabrian Mountains was evidenced by deep seismic reflection and refraction profiles (Pulgar et al., 1996; Fernández-Viejo et al., 2000; Pedreira et al., 2007), with their results being further supported by potential-field modeling (Gallastegui, 2000; Pedreira et al., 2007, 2015). This high-velocity feature is continuous towards the east and ends against the HTZ, agreeing with previous seismic findings of Pedreira et al. (2003). Pedreira et al. (2007) showed the reconstructed trace of the southernmost extent of this lower crustal wedge, based on its identification in the seismic profiles, and in a 3D gravity modeling. This trace is depicted in Figure 8 (lower left panel) for comparison. Our results are remarkably consistent with these previous interpretations, considering the lateral resolution of the model. The V_S values of the crustal wedge are lower toward the central Cantabrian Mountains, approximately beneath the eastern termination of the Paleozoic massif, appearing as a low-velocity anomaly in the relative V_S maps (22-km slice, Figure 8). However, these velocities are nevertheless still higher than the underlying Iberian crust, which also features lower velocities in that area. The indentation is better observed in a N–S direction (Figure 8, section BB′): note how the Iberian Moho deepens beneath the indenter, and how the small high-velocity body at 9–15 km depth is only located on top of the lower crust from the northern domain. This supports previous interpretations of this body as a segment of the lower crust from the European domain thrusted and uplifted towards the north during the indentation and being responsible for the BCMA (Pedreira et al., 2003, 2007).

Our results disagree with recent interpretations that consider the presence of mantle in situ at < 10 km depth approximately beneath the area of the BCMA in Zone 2 (Pedrera et al., 2017; García-Senz et al., 2019). These authors argue that the mantle was exhumed to the base of the sedimentary pile in the Basque-Cantabrian Basin during the Mesozoic, and that the geometry of this mantle uplift was only subtly modified by the orogenic event that gave rise to the Pyrenean-Cantabrian Mountain belt during the Cenozoic. Pedreira et al. (2018) already pointed out that this hypothesis is incompatible with the previous seismic data available in the area. Still, we wanted to derive a representative 1D shear wave profile from this "exhumed mantle model" to test: i) what is the shape of the dispersion curve it predicts; and ii) how the use of substantially different initial models may affect the results of the non-linear inversion. The S-wave velocities of the exhumed mantle rocks can be estimated either from their magnetic properties, which are dependent upon their degree of serpentinization (e.g., Oufi et al., 2002; Maffione et al., 2014), or from their densities (e.g., Christensen, 1996, 2004; Carlson & Miller, 2003). However, there are some inconsistences between the magnetic properties and the densities employed by the authors of the exhumed mantle model (see the comment by Pedreira et al., 2018), so we derived two 1D shear velocity models to use as starting models: one from the "magnetic" model by Pedrera et al. (2017, 2018) and the other from the "gravity" model by García-Senz et al. (2019) (for a detailed description of the derivation of

these models, please see Text S5 and Tables S1 and S2 in the Supporting Information). We then used these models as initial solutions in a nonlinear inversion of the phase velocities compiled at node 1575, which is located above the mantle uplift zone proposed by these authors. The synthetic dispersion curves computed from these two models (blue lines in Figure 9) have much steeper slopes than the observed phase velocities (black dots in Figure 9), as can be expected from placing the mantle at such shallow depths. Moreover, the nonlinear inversion resulted in both cases in best-fitting models (red lines in Figure 9) that do not preserve any of the initial features of the "exhumed mantle" initial models, but rather resemble our own results, developing two shear-wave velocity inversions with depth.

Our model is in a broad sense coherent with previous tomographic studies in the area, altough it provides further details due to its increased resolution. The V_S model obtained by Macquet et al. (2014) through seismic noise cross-correlation in time domain and with minimum interstation distances of 60 km, resembles surface geology at a depth of 5 km, with the outcrops of Paleozoic basement showing the highest velocities. Their estimated V_S values are comparable with those shown in this work, at around 3.2 km/s for the Paleozoic of the Cantabrian Mountains and with the BCZ and Cenozoic basins ranging from ∼2.6 to 2.9 km/s. A local work carried out by Acevedo et al. (2019), on a scale more similar to our own, found velocities of around 3.3 km/s at a depth of 5 km below the Paleozoic outcrops of the Cantabrian Mountains. The Cenozoic sediments can be clearly seen in our cross-section BB′ as the zone with the lowest velocities (Figure 8), although there is not a clear separation between the Rioja Trough, where thicknesses of about 5 km are reached, and the border of the orogenic wedge, where thick Cenozoic sediments are also present both in the hangingwall (Miranda-Treviño syncline) and in the footwall of the low-angle frontal thrust (e.g., Cámara, 2017). Note that the base of the Cenozoic in the Rioja Trough can be located in our model at approximately 5 km depth, which is consistent with the information from the Rioja-3 borehole (located along the BB′ section just ahead of the mountain front), which cuts 5120 m of Cenozoic sediments before reaching the basement (IGME, 1987).

The period-dependent wavelengths, along with data coverage, are the most important factors that determine lateral resolution. The phase velocity maps are coherent with the resolution analysis, as they do not feature any anomalies smaller than the estimated resolution at any period. The BCZ is in the central area of the SISCAN-MISTERIOS network and therefore is the best resolved area at all periods. Data coverage degrades towards the periphery of the seismic network, with the resolution maps featuring some small areas with very large spatial resolution values right on the borders of the studied region. These anomalous high values are an effect of the poor data coverage on the resolution matrix and are not reliable estimates (Barmin et al., 2001).

Some of the choices adopted in the inversion procedure can also have a potential impact on the final velocity model. One is the linearization of the surface-wave propagation problem, which is an important assumption in any large-scale tomographic application. Rawlinson and Spakman (2016) showed that the errors introduced by the linear assumption are small compared with the amplitude of the velocity anomalies in regions of good angular coverage. This assumption holds in our case, since no phase-velocity anomalies with amplitudes exceeding 20 per cent are observed, and the angular coverage is good in the majority of the study area, with only slight degradation toward the periphery (Figure 6).

Another important issue is the choice of initial V_S models and constraints for the nonlinear inversion, as an unconstrained random search of the model space may be very inefficient and yield unacceptable shear-wave velocity models (e.g., Sambridge, 2001). For this reason, we chose to build our initial models after the results of Pedreira et al. (2003). We consider that said results constitute a good starting point for the nonlinear inversion algorithm because (a) they already satisfy a wide-angle reflection/refraction

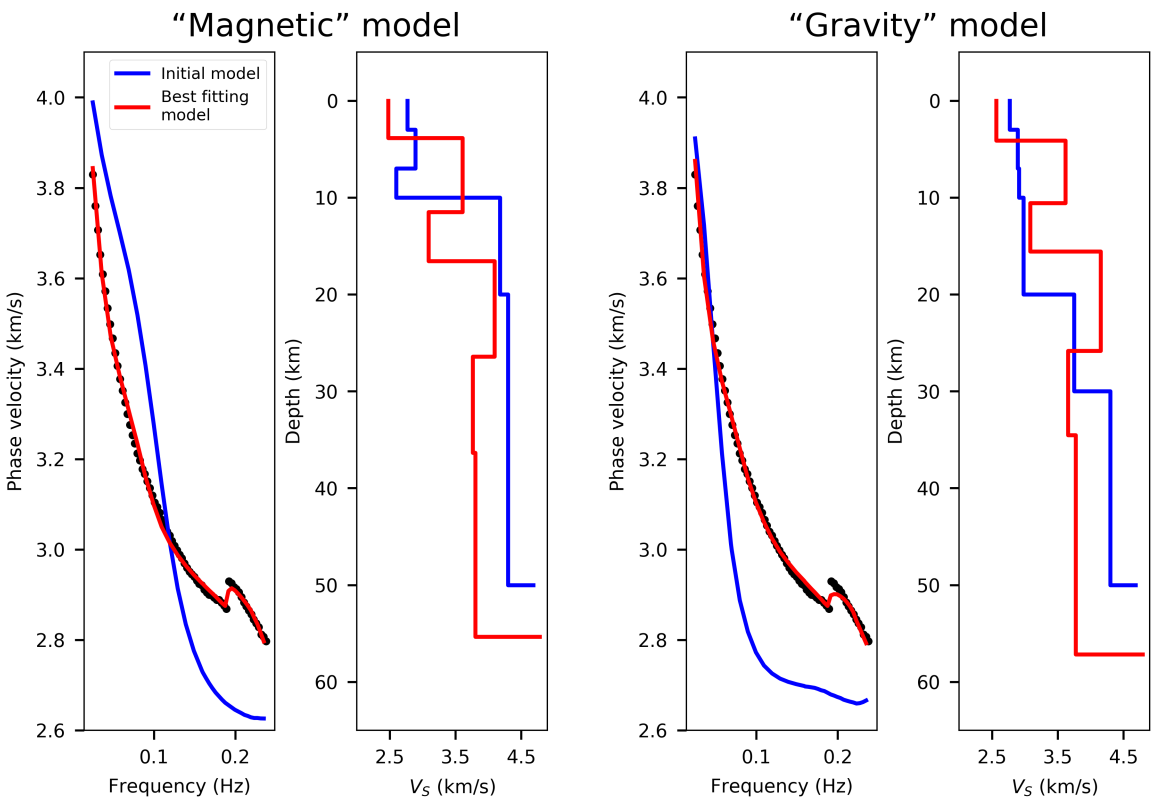

Figure 9. Comparison of the "exhumed mantle" models with the observed phase velocities (black dots) at node 1575 (Eastern Basque-Cantabrian Zone). The blue lines show the initial models derived from the magnetic susceptibilities reported by Pedrera et al. (2017) ("magnetic" model, left, see Table S1 in the Supporting Information) and from the gravity model of García-Senz et al. (2019) ("gravity" model, right, see Table S2 in the Supporting Information) and their associated dispersion curves. Red lines show the outcome of the nonlinear inversion using the "gravity" and "magnetic" model as initial models.

dataset and can explain the gravity and magnetic anomalies over the area (Pedreira et al., 2007); and (b) the synthetic dispersion curves that these initial models yield are in a similar velocity range to the observed values. As explained in section 4, the geographical extents for these initial models (Figure 2) were selected after careful inspection of the shapes of the compiled dispersion curves and considering the pre-existing geological and geophysical knowledge (e.g., Fernández-Viejo et al., 2000; Pedreira et al., 2003, 2007; Quintana et al., 2015; DeFelipe et al., 2017) of the area. In any case, it must be kept in mind that each node within a zone evolves differently from the same starting model, discarding the features that don't satisfy the dataset, and the inversion scheme has been proved to be robust enough to converge into similar results from strongly different initial models (e.g., models of Figure 9). With the aim of preventing geologically and/or physically implausible results, and since a high number of phase velocity measurements are available in the 4–40-s period range, we only impose two restrictions on the solutions: shear-wave velocity inversions are only allowed in those regions in which prior studies support their existence, and Moho depths are only allowed to vary inside a closed, but wide enough range (10-15 km, Table 1). The reasoning behind the latter choice is that the deeper layers of the model (deeper than 35 km) are the least constrained, not only

because the number of measurements decreases towards longer periods (Figure 4), but also because of the increasing wavelengths. For this same reason, we do not discuss here in detail the implications of the Moho depth variations predicted by the model.

The spatial distribution of the seismic noise sources may also have an small effect the phase velocity measurements, as the theory behind current tomographic applications of seismic noise relies in the assumption that the seismic noise wavefield is fully equipartitioned. However, this requirement is often not met, as low-frequency seismic noise primarily arises from oceanic storms (e.g., Díaz, 2016) and therefore will have a preferred direction. For Iberia, Ermert et al. (2016) found a two-sided pattern both around the primary and secondary microseismic peaks, with stronger than average sources in the Atlantic Ocean, particularly along the coast of the Bay of Biscay, and weaker sources in the Western Mediterranean. Since our study area is limited to the north by the Bay of Biscay, it is to be expected that the highest noise intensity would come from the N or NW directions. To corroborate this assumption, we performed a f-k analysis following Gal et al. (2014), centered on the primary microseismic peak frequency using our own dataset. The results of this test show the most intense seismic noise sources being located to the north of the study area, while a sufficient level of noise arises from all azimuthal sectors (for further details see Text S6 and Figure S4 in the Supporting Information). In any case, the non-isotropic nature of the seismic noise wavefield has a very small effect on the measured velocities of surface waves and is not a crucial issue (e.g., Weaver et al., 2009; Froment et al., 2010; Yao & van der Hilst, 2009).

Our results reflect that the method presented in this work has important advantages over the more frequently used time-domain approach. First, the determination of phase velocities of Rayleigh waves does not depend on the far-field approximation (Ekström et al., 2009) and is therefore particularly appropriate for dense seismic networks with closely spaced stations. This provides a consistent data coverage over a wider range of frequencies (Figure 6). Second, the time-domain approach suffers the risk of possible misidentification of higher-mode Rayleigh waves with the fundamental mode (e.g., Tanimoto & Rivera, 2005; Muir & Tsai, 2017), and detailed discrimination between the fundamental mode signal and higher overtones is seldom done. This can lead to important errors when inverting for complex shear-wave velocity structures (Maraschini et al., 2010). By accounting for the possible contribution of higher modes in the forward modeling, we avoid this risk. Furthermore, higher modes provide additional information about the V_S structure and can increase the resolution of the inverted models (Xia et al., 2003). Higher modes are especially sensitive to velocity decreases with depth (Gucunsky & Woods, 1992; Xia et al., 2003), and previous studies have shown that accounting for higher modes might increase the investigation depth (Socco et al., 2010). Finally, in order to properly gather multimode information, the dispersion curves need to be estimated with good resolution (Socco et al., 2010), which is achieved by the waveform fitting procedure (Menke & Jin, 2015). For normally dispersive media, the influence of higher modes over the apparent phase velocity curve can be negligible, and the apparent dispersion curve can be considered equal to the dispersion curve of the fundamental mode (for an example, see Figure S1 in the Supporting Information). Therefore, the approach described in this work is also valid even if no higher modes are present in the dataset.

The most notable example of higher mode contribution in our work is found in the Eastern Basque-Cantabrian Zone (NE of zone Z2, Figure 6), where the dispersion curves compiled from the phase-velocity maps exhibit a small drop at approximately $\sim$0.18 Hz. The multimode nonlinear inversion algorithm achieved a good fit for these dispersion curves (Figure 7, node 1575), with the corresponding shear-wave velocity models depicting an inversion of velocities with depth beneath the high-velocity intracrustal body, coherently with the results of active-source seismic profiling (Pedreira et al., 2003).

7 Conclusions

In this work, we present a new approach for imaging structurally complex regions using ambient seismic noise. This method measures phase velocities from the ambient-noise cross-correlation spectrum and does not depend on the far-field approximation, which makes it appropriate for dense seismic networks with closely spaced stations. By accounting for the contribution of higher modes of Rayleigh waves to the observed phase velocities, additional information is provided to the inversion scheme, achieving better constrained solutions. We apply this methodology to data recorded by the stations of the SISCAN-MISTERIOS network, deployed in the Basque-Cantabrian Zone (BCZ), a complex area affected by several tectonic events with a highly heterogeneous crust. The dense path coverage and the substantial higher-mode content of the data make it possible to build a detailed 3D shear-wave velocity model of the BCZ and surrounding areas, which supports a wide range of previous geophysical and geological observations. The main features of this model are an E–W-trending, high-velocity intracrustal layer in the northern part of the study area which is interpreted as an imbrication of the Cantabrian margin/European lower crust, and a shallow, isolated high-velocity body in the Bilbao area at 9–15 km depth, which could explain the Basque Country Magnetic Anomaly. The dispersion curves in that area show a small jump at around 0.18 Hz, which is linked to the contribution of higher modes of propagation excited by the velocity inversion caused by the presence of the anomalous, shallow high-velocity body. This feature highlights the importance of using methods that can account for additional information when imaging such complex structures. The observed phase velocities have also been shown to be incompatible with recent models proposing the presence of exhumed mantle at < 10 km depth (Pedrera et al., 2017; García-Senz et al., 2019). Future lines of work include incorporating additional datasets in the form of a joint inversion, such as horizontal-to-vertical spectral ratios and receiver functions, which will allow to better constrain the shallow and deeper parts of the models, respectively.

Acknowledgments

Data used in this study will be made available through the FDSN repository cited in the references (Díaz & Pulgar, 2015). We are grateful to our colleagues of the High Energy Physics group of the University of Oviedo for helping us perform our calculations. We thank the Government of the Principality of Asturias and the Spanish Ministry of Education for the PhD financial support given to Andrés Olivar-Castaño, through the "Severo Ochoa" and FPU grants. This research was funded by the Spanish Ministry of Economy and Competitiveness project MISTERIOS (CGL2013-48601-C2-2-R) and the University of Oviedo Foundation project SISCAN (FUO-EM-253-13). This is a contribution of the GEOTEC Group, with additional funding from the European Regional Development Funds and the Government of the Principality of Asturias (IDI/2018/000216).

References

Acevedo, J., Fernández-Viejo, G., Llana-Fúnez, S., & López-Fernández, C. (2019). Ambient noise tomography of the southern sector of the Cantabrian Mountains, NW Spain. *Geophysical Journal International*, *219*, 479-495. doi: 10.1093/gji/ggz308

Aki, K. (1957). Space and time spectra of stationary stochastic waves, with special reference to microtremors. *Bulletin of the Earthquake Research Institute*, *35*, 415-456.

Aki, K., & Richards, P. G. (2002). *Quantitative Seismology* (2nd ed.). University Science Books, Sausalito, California.

Aller, J., & Zeyen, H. J. (1996). A 2.5-d interpretation of the Basque country magnetic anomaly (northern Spain: geodynamical implications. *Geologische Rundschau*, *85*, 303-309.

Alonso, J., Pulgar, J., García-Ramos, J., & Barba, P. (1996). Tertiary basins and alpine tectonics in the Cantabrian Mountains (NW) Spain. In P. Friend & C. Dabrio (Eds.), *Tertiary basins of Spain: The stratigraphic record of crustal kinematics* (Vol. World and Regional Geology 6, p. 2214-227). Cambridge University Press. doi: 10.1017/CBO9780511524851.031

Ardizone, J., Mezcua, J., & Socias, I. (1989). *Mapa aeromagnético de la España peninsular.* Maps 17.344-1989 to 17.346-1989, IGN, Madrid.

Aurell, M., Robles, S., Bádenas, B., Rosales, I., Quesada, S., Meléndez, G., & García-Ramos, J. (2003). Transgressive-regressive cycles and Jurassic palaeogeography of northeast Iberia. *Sedimentary Geology*, *162(3-4)*, 239-271. doi: 10.1016/S0037-0738(03)00154-4

Azambre, B., & Rossy, M. (1976). Le magmatisme alcalin d'âge crétacé dans les Pyrénées occidentales et l'Arc basque, ses relations avec le métamorphisme et la tectonique. *Bulletin de la Société Géologique de France*, *18*, 1725-1728.

Barmin, M. P., Ritzwoller, M. H., & Levshin, A. L. (2001). A fast and reliable method for surface wave tomography. *Pure and Applied Geophysics*, *158*, 1351-1375. doi: 10.1007/PL00001225

Ben-Ameur, W. (2004). Computing the initial temperature of simulated annealing. *Computational Optimization and Applications*, *29*, 369-385.

Ben-Menahem, A., & Singh, S. J. (2000). *Seismic waves and sources.* Springer, New York, NY. doi: 10.1007/978-1-4612-5856-8

Bensen, G. D., Ritzwoller, M. H., Barmin, M. P., Levshin, A. L., Lin, F., Moschetti, M. P., ... Yang, Y. (2007). Processing seismic ambient noise data to obtain reliable broad-band surface wave dispersion measurements. *Geophysical Journal International*, *196*, 1239-1260. doi: 10.1111/j.1365-246X.2007.03374.x

Bonnefoy-Claudet, S., Cotton, F., & Bard, P. Y. (2006). The nature of noise wavefield and its applications for site effects studies, a literature review. *Earth-Science Reviews*, *79*, 205-227. doi: 10.1016/j.earscirev.2006.07.004

Boschi, L., Weemstra, C., Verbeke, J., Ekström, G., Zunino, A., & Giardini, D. (2013). On measuring surface wave phase velocity from station-station cross correlation of ambient signal. *Geophysical Journal International*, *192*, 346-358. doi: 10.1093/gji/ggs023

Carlson, R. L., & Miller, D. J. (2003). Mantle wedge water contents estimated from seismic velocities in partially serpentinized peridotites. *Geophysical Research Letters*, *30 (5)*. doi: 10.1029/2002GL016600

Carola, E., Muñoz, J. A., & Roca, E. (2013). The transition from thick-skinned to thin-skinned tectonics in the Basque-Cantabrian Pyrenees: the Burgalesa Platform and surroundings. *International Journal of Earth Sciences*, *104*, 2215-2239. doi: 10.1007/s00531-015-1177-z

Castañares, L. M., Robles, S., Gimeno, D., & Bravo, J. C. V. (2001). The submarine volcanic system of the Errigoiti formation (Albian-Santonian of the Basque-Cantabrian Basin, northern Spain): stratigraphic framework, facies, and sequences. *Journal of Sedimentary Research*, *71(2)*, 318-333. doi: 10.1306/080700710318

Chevrot, S., Villaseñor, A., Sylvander, M., Benahmed, S., Beucler, E., Cougoulat, G., ... Wolyniec, D. (2014). High-resolution imaging of the Pyrenees and Massif Central from the data of the Pyrope and IBERARRAY portable array deployments. *Journal of Geophysical Research: Solid Earth*, *119*, 6399-6420. doi: 10.1002/2014JB010953

Christensen, N. I. (1996). Poisson's ratio and crustal seismology. *Journal of Geophysical Research*, *101 (B2)*. doi: 10.1029/95JB03446

Christensen, N. I. (2004). Serpentinites, Peridotites, and Seismology. *International Geology Review*, *46*. doi: 10.2747/0020-6814.46.9.795

Cámara, P. (1997). The Basque-Cantabrian basin's Mesozoic tectonosedimentary evolution. *Mémoires de la Société géologique de France*, *171*, 187-191.

Cámara, P. (2017). Salt and Strike-Slip Tectonics as Main Drivers in the Structural Evolution of the Basque-Cantabrian Basin, Spain. In J. I. Soto, J. Flinch, & G. Tari (Eds.), *Permo-Triassic Salt Provinces of Europe, North Africa and the Atlantic Margins* (Vol. Tectonics and Hydrocarbon Potential 17). Elsevier. doi: 10.1016/B978-0-12-809417-4.00018-5

Díaz, J. (2016). On the origin of the signals observed across the seismic spectrum. *Earth-Science Reviews*, *161*, 224-232. doi: 10.1016/j.earscirev.2016.07.006

Díaz, J., Pedreira, D., Ruiz, M., Pulgar, J. A., & Gallart, J. (2012). Mapping the indentation between the Iberian and Eurasian plates beneath the Western Pyrenees/Eastern Cantabrian Mountains from receiver function analysis. *Tectonophysics*, *570-571*, 114-122. doi: 10.1016/j.tecto.2012.07.005

Díaz, J., & Pulgar, J. A. (2015). *MISTERIOS.* International Federation of Digital Seismograph Networks, Dataset/Seismic Network, doi:10.7914/SN/2M_2015.

DeFelipe, I., Pedreira, D., Pulgar, J. A., Iriarte, E., & Mendia, M. (2017). Mantle exhumation and metamorphism in the Basque-Cantabrian Basin (N Spain): Stable and clumped isotope analysis in carbonates and comparison with ophicalcites in the North-Pyrenean Zone (Urdach and Lherz). *Geochemistry, Geophysics, Geosystems*, *18*, 631-652. doi: 10.1002/2016GC006690

Ekström, G. (2014). Love and Rayleigh phase velocity maps, 5-40 s, of the western and central usa from usarray data. *Earth and Planetary Science Letters*, *402*, 42-49. doi: 10.1016/j.epsl.2013.11.022

Ekström, G., Abers, G. A., & Webb, S. C. (2009). Determination of surface wave phase velocities across usarray from noise and aki's spectral formulation. *Geophysical Research Letters*, *36*, 5-9. doi: 10.1029/2009GL039131

Ermert, L., Villaseñor, A., & Fitchner, A. (2016). Cross-correlation imaging of ambient noise sources. *Geophysical Journal International*, *204 (1)*, 347-364. doi: 10.1093/gji/ggv460

Fernández-Viejo, G., Gallart, J., Pulgar, J. A., Córdoba, D., & Dañobeitia, J. J. (2000). Seismic signature of Variscan and Alpine tectonics in NW Iberia: crustal structure of the Cantabrian Mountains and Duero basin. *Journal of Geophysical Research: Solid Earth*, *105*, 3001-3018. doi: 10.1029/1999JB900321

Fillon, C., Pedreira, D., van der Beek, P. A., Huismans, R. S., Barbero, L., & Pulgar, J. A. (2016). Alpine exhumation of the central Cantabrian Mountains, Northwest Spain. *Tectonics*, *35(2)*, 339-356. doi: 10.1002/2015TC004050

Froment, B., Campillo, M., Roux, P., Gouedard, P., Verdel, A., & Weaver, R. L. (2010). Estimation of the effect of nonisotropically distributed energy on the apparent arrival time in correlations. *Geophysics*, *75 (5)*, SA85-SA93. doi: 10.1190/1.3483102

Gal, M., Reading, A. M., Ellingsen, S. P., Koper, K. D., Gibbons, S. J., & Näsholm, S. P. (2014). Improved implementation of the fk and capon methods for array analysis of seismic noise. *Geophysical Journal International*, *198 (2)*, 1045-1054. doi: 10.1093/gji/ggu183

Gallastegui, J. (2000). Estructura cortical de la cordillera y margen continental cantábricos. *Trabajos de Geología (in Spanish)*, *22*, 9-234.

García-Jerez, A., Piña-Flores, J., Sánchez-Sesma, F. J., Luzón, F., & Perton, M. (2016). A computer code for forward calculation and inversion of the H/V spectral ratio under the diffuse field assumption. *Computers & Geosciences*, *97*, 67-78. doi: 10.1016/j.cageo.2016.06.016

García-Mondejar, J., Agirrezabala, L. M., Aranburu, A., Fernández-Mendiola, P. A., Gómez-Pérez, I., López-Horgue, M., & Rosales, I. (1996). Aptial-Albian tectonic pattern of the basque-cantabrian basin (northern Spain). *Geological Journal*, *31*, 13-45. doi: 10.1002/(SICI)1099-1034(199603)31:113::AID-GJ6893.0.CO;2-Y

García-Senz, J., Pedrera, A., Ayala, C., Ruiz-Constán, A., Robador, A., &

Rodríguez-Fernández, L. R. (2019). Inversion of the north Iberian hyper-extended margin: the role of exhumed mantle indentation during continental collision. *Tectonics*, *36 (12)*, 3155-3177. doi: 10.1002/2017TC004716

Goutorbe, B., Oliveira Coelho, D. L., & Drouet, S. (2015). Rayleigh wave group velocities at periods of 6-23 s across Brazil from ambient noise tomography. *Geophysical Journal International*, *203*, 869-882. doi: 10.1093/gji/ggv343

Gucunsky, N., & Woods, R. D. (1992). Numerical simulation of the SASW test. *Soil Dynamics and Earthquake Engineering*, *11(4)*, 213-227. doi: 10.1016/0267-7261(92)90036-D

Harkrider, D. G. (1964). Surface waves in multilayered elastic media I. Rayleigh and Love waves from buried sources in a multilayered elastic half-space. *Bulletin of the Seismological Society of America*, *54(2)*, 627-679.

Harkrider, D. G., & Anderson, D. L. (1966). Surface wave energy from point sources in plane layered Earth models. *Journal of Geophysical Research*, *71(12)*, 2967-2980. doi: 10.1029/JZ071i012p02967

Haskell, N. A. (1953). The dispersion of surface waves on multilayered media. *Bulletin of the Seismological Society of America*, *43(1)*, 17-34.

IGME. (1987). *Contribución de la exploración petrolífera al conocimiento de la Geología de España*. Instituto Geológico y Minero de España (IGME), Servicio de Publicaciones, Madrid.

Kirkpatrick, S. (1984). Optimization by Simulated Annealing: Quantitative studies. *Journal of Statistical Physics*, *34(5-6)*, 975-986. doi: 10.1007/BF01009452

Kirkpatrick, S., Gelatt Jr., C. D., & Vecchi, M. P. (1983). Optimization by Simulated Annealing. *Science*, *220(4598)*, 671-680. doi: 10.1126/science.220.4598.671

Larrasoaña, J. C., Parés, J. M., Millán, H., del Valle, J., & Pueyo, E. L. (2003). Paleomagnetic, structural and stratigraphic constraints on transverse fault kinematics during basin inversion: The Pamplona Fault (Pyrenees, north Spain). *Tectonics*, *22(6)*, 1071. doi: 10.1029/2002TC001446

Levsin, A. L., Yanovskaya, T. B., Lander, A. V., Bukchin, B. G., Barmin, M. P., Ratnikova, L. I., & Its, E. N. (1989). *Seismic surface waves in a laterally inhomogeneous earth* (V. I. Keilis-Borok, Ed.). Kluwer Academic Publishers, London.

Lin, F. C., Moschetti, M., & Ritzwoller, M. H. (2008). Surface wave tomography of the western United States from ambient seismic noise: Rayleigh and Love wave phase velocity maps. *Geophysical Journal International*, *173*, 281-298. doi: 10.1111/j.1365-246X.2008.03720.x

Lin, F. C., Ritzwoller, M. H., Townend, J., Bannister, S., & Savage, M. K. (2007). Ambient noise Rayleigh wave tomography of New Zealand. *Geophysical Journal International*, *170*, 649-666. doi: 10.1111/j.1365-246X.2008.03414.x

Lobkis, O. I., & Weaver, R. L. (2001). On the emergence of the green's function in the correlations of a diffuse field. *Journal of the Acoustical Society of America*, *110*, 3011-3017. doi: 10.1121/1.1417528

López-Gómez, J., Martín-González, F., Heredia, N., de la Horra, R., Barrenechea, J. F., Cadenas, P., ... Gand, G. (2019). New lithostratigraphy for the Cantabrian Mountains: A common tectonostratigraphic evolution for the onset of the Alpine cycle in the W Pyrenean realm, N Spain. *Earth-Science Reviews*, *188*, 249-271. doi: 10.1016/j.earscirev.2018.11.008

Luo, Y., Yang, Y., Xu, Y., Xu, H., Zhao, K., & Wang, K. (2015). On the limitations of interstation distances in ambient noise tomography. *Geophysical Journal International*, *201*, 652-661. doi: 10.1093/gji/ggv043

Macquet, M., Paul, A., Pedersen, H. A., Villaseñor, A., Chevrot, S., Sylvander, M., & Wolyniec, D. (2014). Ambient noise tomography of the Pyrenees and the surrounding regions: inversion for a 3-D Vs model in the presence of a very heterogeneous crust. *Geophysical Journal International*, *199*, 402-415. doi:

10.1093/gji/ggu270

Maffione, M., Morris, A., Plümper, O., & van Hinsbergen, D. J. J. (2014). Magnetic properties of variably serpentinized peridotites and their implication for the evolution of oceanic core complexes. *Geochemistry, Geophysics, Geosystems*, *15*, 923-944. doi: 10.1002/2013GC004993

Maraschini, M., Ernst, F., Foti, S., & Socco, L. V. (2010). A new misfit function for multimodal inversion of surface waves. *Geophysics*, *75(4)*, G31-G43. doi: 10.1190/1.3436539

Menke, W. (2012). *Geophysical Data Analysis: Discrete Inverse Theory, MATLAB Edition*. Elsevier, New York, NY.

Menke, W., & Jin, G. (2015). Waveform fitting of cross spectra to determine phase velocity using Aki's formula. *Bulletin of the Seismological Society of America*, *105*, 1619-1627. doi: 10.1785/0120140245

Muir, V., & Tsai, V. C. (2017). Rayleigh-wave H/V via noise cross correlation in southern California. *Bulletin of the Seismological Society of America*, *107(5)*, 2021-2027. doi: 10.1785/0120170051

Ohori, M., Nobata, A., & Wakamatsu, K. (2002). A comparison of ESAC and FK methods of estimating phase velocity using arbitrarily shaped microtremor arrays. *Bulletin of the Seismological Society of America*, *92*, 2323-2332. doi: 10.1785/0119980109

Omodeo-Salé, S., Salas, R., Guimerà, J., Ondrak, R., Mas, R., Arribas, J., ... Martinez, L. (2015). Subsidence and thermal history of an inverted late jurassic-early cretaceous extensional basin (Cameros, North-central Spain affected by very low- to low-grade metamorphism. *Basin Research*, *29 (S1)*, 156-174. doi: 10.1111/bre.12142

Oufi, O., Cannat, M., & Horen, H. (2002). Magnetic properties of variably serpentinized abyssal peridotites. *Journal of Geophysical Research - Solid Earth*, *107 (B5)*, EPM 3-1-EPM 3-19. doi: 10.1029/2001JB000549

Palomeras, I., Villaseñor, A., Thurner, S., Levander, A., Gallart, J., & Harnafi, M. (2017). Lithospheric structure of Iberia and Morocco using finite-frequency Rayleigh wave tomography from earthquakes and seismic ambient noise. *Geochemistry, Geophysics, Geosystems*, *18(5)*, 1824-1840. doi: 10.1002/2016GC006657

Park, C. B., Miller, R. D., & Xia, J. (2000). Detection of higher mode surface waves over unconsolidated sediments by the MSAW method. *Symposium on the Application of Geophysics to Engineering and Environmental Problems 2000*. doi: 10.4133/1.2922744

Parolai, S., Picozzi, M., Richwalski, S. M., & Milkereit, C. (2005). Joint inversion of phase velocity dispersion and H/V ratio curves from seismic noise recordings using a genetic algorithm, considering higher modes. *Geophysical Research Letters*, *32*, L01303. doi: 10.1029/2004GL021115

Pedreira, D. (2005). *Estructura cortical de la zona de transición entre los Pirineos y la Cordillera Cantábrica. PhD Thesis (2004)*. Ed. Universidad de Oviedo (Ediuno), ISBN: 84-8317-528-2, 343 pp.

Pedreira, D., Afonso, J. C., Pulgar, J. A., Gallastegui, J., Carballo, A., Fernàndez, M., ... García-Moreno, O. (2015). Geophysical-petrological modeling of the lithosphere beneath the Cantabrian Mountains and the North-Iberian margin: geodynamic implications. *Lithos*, *230*, 46-68. doi: 10.1016/j.lithos.2015.04.018

Pedreira, D., Pulgar, J. A., Díaz, J., Alonso, J. L., Gallastegui, J., & Teixell, A. (2018). Comment on "Reconstruction of the Exhumed Mantle Across the North Iberian Margin by Crustal-Scale 3-D Gravity Inversion and Geological Cross Section" by Pedrera et al. *Tectonics*, *37*, 4338-4345. doi: 10.1029/2018TC005129

Pedreira, D., Pulgar, J. A., Gallart, J., & Díaz, J. (2003). Seismic evidence of Alpine

crustal thickening and wedging from the western Pyrenees to the Cantabrian Mountains (north Iberia). *Journal of Geophysical Research*, *108*, B42204. doi: 10.1029/2001JB001667

Pedreira, D., Pulgar, J. A., Gallart, J., & Torné, M. (2007). Three-dimensional gravity and magnetic modeling of crustal indentation and wedging in the western Pyrenees-Cantabrian Mountains. *Journal of Geophysical Research*, *112*, B12405. doi: 10.1029/2007JB005021

Pedrera, A., García-Senz, J., Ayala, C., Ruiz-Constán, A., Rodríguez-Fernández, L. R., Robador, A., & González Menéndez, L. (2017). Reconstruction of the Exhumed Mantle Across the North Iberian Margin by Crustal-Scale 3-D Gravity Inversion and Geological Cross Section. *Tectonics*, *36 (12)*, 3155-3177. doi: 10.1002/2017TC004716

Pedrera, A., García-Senz, J., Ayala, C., Ruiz-Constán, A., Rodríguez-Fernández, L. R., Robador, A., & González Menéndez, L. (2018). Reply to Comment by Pedreira et al. on "Reconstruction of the Exhumed Mantle Across the North Iberian Margin by Crustal-Scale 3-D Gravity Inversion and Geological Cross Section". *Tectonics*, *37*. doi: 10.1029/2018TC005222

Pilz, M., Parolai, S., Picozzi, M., & Bindi, D. (2012). Three-dimensional shear wave velocity imaging by ambient seismic noise tomography. *Geophysical Journal International*, *189*, 501-502. doi: 10.1111/j.1365-246X.2011.05340.x

Pilz, M., Parolai, S., & Woith, H. (2017). A 3-D algorithm based on the combined inversion of Rayleigh and Love waves for imaging and monitoring of shallow structures. *Geophysical Journal International*, *209*, 152-166. doi: 10.1093/gji/ggx005

Poli, P., Campillo, M., Pedersen, H., & the LAPNET Working Group. (2012). Body-wave imaging of Earth's mantle discontinuities from ambient seismic noise. *Science*, *371*, 1063-1066. doi: 10.1126/science.1228194

Prieto, G. A., Lawrence, J. F., & Beroza, G. C. (2009). Anelastic Earth structure from the coherency of the ambient seismic field. *Journal of Geophysical Research*, *114*, B07303. doi: 10.1029/2008JB006067

Pulgar, J. A., Gallart, J., Fernández-Viejo, G., Pérez-Estaún, A., Álvarez Marrón, J., & the ESCIN Group. (1996). Seismic image of the Cantabrian Mountains in the western extension of the pyrenees from integrated ESCIN reflection and refraction data. *Tectonophysics*, *264*, 1-19.

Quintana, L., Pulgar, J. A., & Alonso, J. L. (2015). Displacement transfer from borders to interior of a plate: A crustal transect of Iberia. *Tectonophysics*, *663*, 378-398. doi: 10.1016/j.tecto.2015.08.046

Rat, P. (1988). The Basque-Cantabrian basin between the Iberian and European plates, some facts but still many problems. *Revista de la Sociedad Geológica de España*, *1(3-4)*, 327-348.

Rawlinson, N., & Spakman, W. (2016). On the use of sensitivity test in seismic tomography. *Geophysical Journal International*, *205*, 1221-1243. doi: 10.1093/gji/ggw084

Ritzwoller, M. H., & Levshin, A. L. (1998). Eurasian surface-wave tomography: Group velocities. *Journal of Geophysical Research - Solid Earth*, *103*, 4839-4878. doi: 10.1029/97JB02622

Roca, E., Muñoz, J. A., Ferrer, O., & Ellouz, N. (2011). The role of the Bay of Biscay Mesozoic extensional structure in the configuration of the pyrenean orogen: Constraints from the marconi deep seismic reflection survey. *Tectonics*, *30*, 1-33. doi: 10.1029/2010TC002735

Ruiz, M., Gallart, J., Díaz, J., Olivera, C., Pedreira, D., López, C., ... Pulgar, J. A. (2006). Seismic activity at the western Pyrenean edge. *Tectonophysics*, *412*, 217-235. doi: 10.1016/j.tecto.2005.10.034

Sambridge, M. (2001). Finding acceptable models in nonlinear inverse problems using a neighbourhood algorithm. *Inverse Problems*, *17*, 387-403. doi: 10.1088/

0266-5611/17/3/302

Saygin, E., & Kennett, B. L. N. (2010). Ambient seismic noise tomography of the Australian continent. *Tectonophysics*, *481*, 116-125. doi: 10.1016/j.tecto.2008.11.013

Schwab, F., & Knopoff, L. (1970). Surface wave dispersion computations. *Bulletin of the Seismological Society of America*, *60*, 321-344.

Shapiro, N. M., & Campillo, M. (2004). Emergence of broadband rayleigh waves from correlations of the ambient seismic noise. *Geophysical Research Letters*, *31*, 8-11. doi: 10.1029/2004GL019491

Shapiro, N. M., Singh, S. K., Almora, D., & Ayala, M. (2001). Evidence of the dominance of higher-mode surface waves in the lake-bed zone of the Valley of Mexico. *Geophysical Journal International*, *147*, 517-527. doi: 10.1046/j.0956540x.2001.01508.x

Silveira, G., Afonso Dias, N., & Villaseñor, A. (2013). Seismic imaging of the western Iberian crust using ambient noise: Boundaries and internal structure of the Iberian Massif. *Tectonophysics*, *589*, 186-194. doi: 10.1016/j.tecto.2012.12.025

Socco, L., Foti, S., & Boiero, D. (2010). Surface-wave analysis for building near-surface velocity models - Established approaches and new perspectives. *Geophysics*, *75(5)*, 75A83-75A102. doi: 10.1190/1.3479491

Tang, X. M., Li, C., & Patterson, D. J. (2010). A curve-fitting technique for determining dispersion characteristics of guided elastic waves. *Geophysics*, *75*, 153-160. doi: 10.1190/1.3420736

Tanimoto, T., & Rivera, L. (2005). Prograde Rayleigh wave particle motion. *Geophysical Journal International*, *162*, 399-405. doi: 10.1111/j.1365-246X.2005.02481.x

Tokimatsu, K., Tamura, S., & Kojima, H. (1992). Effects of multiple modes on Rayleigh wave dispersion characteristics. *Journal of Geotechnical Engineering*, *118(10)*, 1529-1543. doi: 10.1061/(ASCE)0733-9410(1992)118:10(1529)

Vidal, M. D. P. C. (2010). Review of the Upper Jurassic-Lower Cretaceous stratigraphy in Western Cameros basin, Northern Spain. *Revista de la Sociedad Geológica de España*, *23(2-3)*, 101-143.

Villaseñor, A., Yang, Y., Ritzwoller, M. H., & Gallart, J. (2007). Ambient noise surface wave tomography of the Iberian Peninsula: implications for shallow seismic structure. *Geophysical Research Letters*, *34*, L11304. doi: 10.1029/2007GL030164

Wang, R. (1999). A simple orthonormalization method for stable and efficient computation of green's functions. *Bulletin of the Seismological Society of America*, *89(3)*, 733-741.

Weaver, R., Froment, B., & Campillo, M. (2009). On the correlation of non-isotropically distributed ballistic scalar diffuse waves. *The Journal of the Acoustical Society of America*, *126 (4)*, 1817-1826. doi: 10.1121/1.3203359

Xia, R., Miller, R. D., Park, C. B., & Tian, G. (2003). Inversion of high frequency surface waves with fundamental and higher modes. *Journal of Applied Geophysics*, *52*, 45-57. doi: 10.1016/S0926-9851(02)00239-2

Yang, Y., Ritzwoller, M. H., Levshin, A. L., & Shapiro, N. M. (2007). Ambient noise Rayleigh wave tomography across Europe. *Geophysical Journal International*, *168*, 259-274. doi: 10.1111/j.1365-246X.2006.03203.x

Yao, H., & van der Hilst, R. D. (2009). Analysis of ambient noise energy distribution and phase velocity bias in ambient noise tomography, with application to se tibet. *Geophysical Journal International*, *179*, 1113-1132. doi: 10.1111/j.1365-246X.2009.04329.x

Supporting Information for "Regional Crustal Imaging by Inversion of Multi-mode Rayleigh Wave Dispersion Curves Measured from Seismic Noise: Application to the Basque-Cantabrian Zone (N Spain)"

A. Olivar-Castaño[1], M. Pilz[2], D. Pedreira[1], J. A. Pulgar[1], A. Díaz-González[1], J. M. González-Cortina[1]

[1]Department of Geology, University of Oviedo, C/Jesús Arias de Velasco S/N, 33005, Oviedo, Spain

[2]Helmholtz Centre Potsdam, GFZ German Research Centre for Geosciences, Telegrafenberg, 14473, Potsdam, Germany

Contents of this file

Introduction

Texts S1 to S4 in this supplementary document contain a detailed description of the methodology presented in the main paper. Text S5 contains a description of the derivation of two 1D shear-wave velocity models for the "exhumed mantle" hypothesis (the numerical values for these models are given in Tables S1-S2). Text S6 contains a brief description of the directionality of the seismic noise in the Basque-Cantabrian Zone. Figure S1 shows two examples of the influence of the higher modes of Rayleigh waves in the apparent

dispersion curve in relation to the medium response functions. Figures S2 and S3 are an example of the influence of the different processing parameters over the linearized travel-time inversion procedure. Figure S4 shows the results of the f-k analysis described in Text S6. All of the references provided in this supplement are cited and included in the reference list of the main text.

Text S1

Determination of Rayleigh Wave Phase Velocities

For a stochastic, stationary wavefield in both space and time, the azimuthally averaged cross spectrum $\bar{\rho}(r,\omega)$ for a receiver separation r and frequency ω behaves as a first-kind Bessel function (Aki, 1957; Ohori et al., 2002):

$$\bar{\rho}(r,\omega) = J_0\left(\frac{\omega}{c(\omega)}r\right) \quad , \tag{1}$$

where $c(\omega)$ is the phase velocity at frequency ω. Ekström (2014) states that the azimuthally averaged cross spectrum $\bar{\rho}(r,\omega)$ can be replaced by the time-averaged cross spectrum obtained for individual station pairs $\rho^S_{ij}(\omega)$. Using the displacement spectra $u(\omega)$ for each pair of stations i, j and time window k the cross-correlation spectrum ρ_{ijk} can be computed as (Ekström, 2014):

$$\rho_{ijk}(\omega) = \frac{u_{ik}(\omega)u^*_{jk}(\omega)}{\sqrt{u_{ik}(\omega)u^*_{ik}(\omega)}\sqrt{u_{jk}(\omega)u^*_{jk}(\omega)}} \quad , \tag{2}$$

where the superscript * indicates the complex conjugate. The resulting cross-correlation spectra are then stacked for each station pair as:

$$\rho^S_{ij}(\omega) = \sum_{k=1}^{k=N} \rho_{ijk}(\omega) \quad , \tag{3}$$

where N is the total number of windows available for the station pair i,j. Since equation (1) describes the complete shape of the observed cross spectrum as a function of the

frequency ω and the phase velocity $c(\omega)$, the determination of the latter lends itself well to a waveform fitting process. The two-step iterative waveform fitting procedure described by Menke and Jin (2015), shown schematically in Figure 5 in the main text, introduces an amplitude factor A into equation (1):

$$\bar{\rho}(r,\omega) = AJ_0\left(\frac{\omega}{c(\omega)}r\right) \quad , \tag{4}$$

in order to account for attenuation and normalization errors in the cross spectrum. The first step is to find initial estimates for the phase velocity $\mathbf{c}(\omega)$ and amplitude factor A, which are denoted $\mathbf{c}(\omega)^0$ and A^0, respectively. These initial estimates can be determined through a standard grid search (e.g., Prieto et al., 2009) as the one that minimizes the L2 error between the observed and predicted cross spectra. Once an initial $\mathbf{c}(\omega)^0$ has been found, A^0 can be computed by least-squares minimization (Menke & Jin, 2015). The second step consist of refining the initial estimates by iterative least-squares regression. The relationship shown in equation (4) can be linearized around a certain estimate solution $\mathbf{m}^{(p)} = [\mathbf{c}(\omega)^p, A^p]$, leading to the linear equation:

$$\mathbf{G}\Delta\mathbf{m} = \Delta\boldsymbol{\rho} \quad , \tag{5}$$

where $\mathbf{G}$ is the data kernel, $\Delta\mathbf{m} = \mathbf{m} - \mathbf{m}^{(p)}$ is the difference between the refined solution and the estimate, and $\Delta\boldsymbol{\rho} = \boldsymbol{\rho}^{obs} - \boldsymbol{\rho}^{pre}(\mathbf{m}^{(p)})$ is the difference between the observed cross-spectrum and the one predicted using the estimate $\mathbf{m}^{(p)}$ and equation (4). The regularization scheme used by Menke and Jin (2015) consists of adding two additional constraints. The first one, $\mathbf{m}^A \approx \mathbf{m}^{(p)}$, prevents the refined result from deviating too much from a certain model $\mathbf{m}^A$, whose choice will be discussed later. The second, $\mathbf{Dm} \approx 0$, imposes smoothness on the refined solution, with $\mathbf{D}$ being the discrete form of the second

derivative operator. The complete generalized least-squares equation takes the form:

$$\begin{bmatrix} \sigma_d^{-1}\mathbf{G} \\ \sigma_A^{-1}\mathbf{I} \\ \sigma_D^{-1}\mathbf{D} \end{bmatrix} \Delta\mathbf{m} = \begin{bmatrix} \sigma_d^{-1}\Delta\boldsymbol{\rho} \\ \sigma_A^{-1}(\mathbf{m}^A - \mathbf{m}^{(p)}) \\ \sigma_D^{-1}\mathbf{D}\mathbf{m}^{(p)} \end{bmatrix} \quad , \tag{6}$$

where $\sigma_d^{-1}, \sigma_A^{-1}, \sigma_D^{-1}$ are the weights assigned to each equation. For the discrete form of the matrices $\mathbf{G}$ and $\mathbf{D}$ and discussion of the choice of weights, we refer the reader to the original article by Menke and Jin (2015). At each step, the new estimate solution is computed as $\mathbf{m}^{(p+1)} = \mathbf{m}^{(p)} + \Delta\mathbf{m}$ and the data kernel $\mathbf{G}$ is updated. This process continues until $\Delta\mathbf{m}$ is sufficiently small (i.e., less than 1% of $\mathbf{m}^{(p)}$).

The choice of $\mathbf{m}^A = [\mathbf{c}(\omega)^A, A^A]$ for the second equation in equation (6) can have a notable influence on the final solution, and therefore is of great importance. Using the estimate obtained in the grid search, $\mathbf{m}^A = [\mathbf{c}(\omega)^0, A^0]$ can introduce unrealistic features in the refined estimate. Menke and Jin (2015) propose to use instead a linear fit of $\mathbf{c}(\omega)^0$ as $\mathbf{c}(\omega)^A$. However, we propose to subtitute $\mathbf{c}(\omega)^0$ for a custom exponential curve, as we find that it can more realistically mimic the behavior of surface wave dispersion (e.g., Tang et al., 2010; Pilz et al., 2017):

$$\mathbf{c}(\omega)^A = d\ \tanh^{-1}(e\,\omega) + \frac{f}{\sqrt{\omega}} \quad , \tag{7}$$

where d, e, and f are constant parameters chosen in such a way that $\mathbf{c}(\omega)^A$ best fits $\mathbf{c}(\omega)^0$, which can be easily found through trial and error (i.e., any Monte Carlo method). Finally, the covariance of the estimated solution can be approximated as (Menke & Jin, 2015):

$$\mathbf{C}_m = \left(\begin{bmatrix} \sigma_d^{-1}\mathbf{G} \\ \sigma_A^{-1}\mathbf{I} \\ \sigma_D^{-1}\mathbf{D} \end{bmatrix}^T \begin{bmatrix} \sigma_d^{-1}\mathbf{G} \\ \sigma_A^{-1}\mathbf{I} \\ \sigma_D^{-1}\mathbf{D} \end{bmatrix} \right)^{-1} . \tag{8}$$

Text S2

Computation of Phase Velocity Maps

The travel-time inversion procedure described by Barmin et al. (2001) uses a grid of nodes to parameterize velocities across the study area. Delaunay triangles are constructed for the grid, and the value of the velocity at any given point $m(\mathbf{r})$ is computed as

$$m(\mathbf{r}) = \sum_{j=1}^{M} m(\mathbf{r}_j) w_j(\mathbf{r}) \ , \tag{9}$$

where M is the number of nodes defining the model, and $\mathbf{r}_j$ their locations. The weights $w_j(\mathbf{r})$ are computed as the barycentric coordinates of the triangle enclosing r, and are zero for the nodes outside of it. The problem of surface wave propagation is linearized by treating surface waves as rays traveling along the great circle paths linking sources and receivers, and therefore the relationship between the data and model-parameter vectors can be written as:

$$\mathbf{Gm} = \mathbf{d} \ , \tag{10}$$

where the data vector $\mathbf{d}$ contains the travel time perturbations between source and receiver and the parameter vector $\mathbf{m}$ contains the slowness perturbations along the nodes, both of them relative to a reference model $\mathbf{c}_0(\mathbf{r})$. The vector $\mathbf{m}$ is estimated by minimization of the penalty function (Barmin et al., 2001; Goutorbe et al., 2015):

$$E(\mathbf{m}) = (\mathbf{Gm} - \mathbf{d})^T \mathbf{C}^{-1} (\mathbf{Gm} - \mathbf{d}) + \alpha^2 ||\mathbf{Fm}||^2 + \beta^2 ||\mathbf{Hm}||^2 \ , \tag{11}$$

The first term of the penalty function represents data misfit. The covariance matrix $\mathbf{C}$ is a diagonal matrix whose non-zero elements are the variances of the observed travel times, which can be estimated from the variance of the phase-velocity curves obtained from the waveform fitting procedure. The second and third terms incorporate the regularization constraints for the inversion. The term $\alpha^2 ||\mathbf{Fm}||^2$ is a spatial smoothing condition, with

matrix $\mathbf{F}$ defined as:

$$F_{ij} = \begin{cases} 1 & \text{if } \ i = j, \ \text{ and} \\ -S(\mathbf{r}_i, \mathbf{r}_j) & \text{if } \ i \neq j \ . \end{cases} \tag{12}$$

In this matrix, S is a smoothing kernel defined as:

$$S(\mathbf{r}_i, \mathbf{r}_j) = \exp\left(-\frac{|\mathbf{r}_i - \mathbf{r}_j|^2}{2\sigma^2}\right), \tag{13a}$$

$$\int_S S(\mathbf{r}_i) dr_j = 1 \ . \tag{13b}$$

where $\mathbf{r}_i$ and $\mathbf{r}_j$ are the positions of the i-th and j-th nodes, respectively, and σ is the spatial correlation parameter. The term $\beta^2||\mathbf{Hm}||^2$ penalizes deviations from the reference model $c_0(\mathbf{r})$ depending on the number of paths crossing the different parts of the model. The weighting function $\mathbf{H}$ is chosen to approach unity in areas of poor coverage and zero otherwise, taking the form (Goutorbe et al., 2015):

$$H_{ij} = \exp(-\lambda\rho_i)\delta_{ij} \ , \tag{14}$$

where the path density ρ is defined as the number of rays intersecting a circle of fixed radius centered at the i-th node of the grid, and the parameter λ controls the sharpness of the weighting function. With these definitions, the relationship between the model and data vectors is:

$$\mathbf{m} = (\mathbf{G}^T\mathbf{C}^{-1}\mathbf{G} + \mathbf{Q})^{-1}\mathbf{G}^T\mathbf{C}^{-1}\mathbf{d} \ , \tag{15}$$

where the matrix $\mathbf{Q}$ includes both regularization constraints:

$$\mathbf{Q} = \alpha^2\mathbf{F}^T\mathbf{F} + \beta^2\mathbf{H}^T\mathbf{H} \ . \tag{16}$$

The covariance matrix associated with the model parameters can be estimated as (Goutorbe et al., 2015):

$$\mathbf{cov}(\mathbf{m}) = (\mathbf{G}^T\mathbf{C}^{-1}\mathbf{G} + \mathbf{Q})^{-1} \ . \tag{17}$$

Text S3

Resolution Analysis

Spatial resolution, interpreted as the minimum distance at which two different point anomalies can be resolved, is estimated starting from the model resolution matrix R, which is computed as (Barmin et al., 2001):

$$\mathbf{R} = (\mathbf{G}^T\mathbf{C}^{-1}\mathbf{G} + \mathbf{Q})^{-1}\mathbf{G}^T\mathbf{C}^{-1}\mathbf{G} \tag{18}$$

where the i-th row of the model resolution matrix $\mathbf{R}$ can be interpreted as the model the inversion would produce if there was a point-like velocity anomaly located at node i (Goutorbe et al., 2015). A cone is fitted to each of these hypothetical models, and the radius of the cone is reported as the spatial resolution at the corresponding grid node. By definition, the spatial resolution value at a given node can never be less than twice the inter-node spacing (Barmin et al., 2001).

Text S4

Forward Modeling of the Apparent Rayleigh Wave Dispersion Curves

Rayleigh wave dispersion curves are computed using the matrix propagator method (Haskell, 1953), in which the Earth is represented by a stack of layers overlying a homogeneous half-space. As the original method is prone to numerical instabilities (Schwab & Knopoff, 1970; Aki & Richards, 2002), we implement the orthonormalization scheme described by Wang (1999). The numerical difficulties are caused by operations between different increasing exponentials. Wang (1999) solves this issue by reconstructing the displacement-stress vector bases from depth to depth and making them orthonormal so that there are no operations between the increasing exponential terms. The vector bases

are defined at the half-space as:

$$\hat{\mathbf{Y}}_n = \mathbf{L}_n \hat{\mathbf{C}}_n \ , \tag{19}$$

where $\mathbf{L}_n$ is the 4×4 layer matrix (Aki & Richards, 2002):

$$\mathbf{L}_n = \begin{pmatrix} \alpha_n k & \beta_n \nu_n & \alpha_n k & \beta_n \nu_n \\ \alpha_n \gamma_n & \beta_n k & -\alpha_n \gamma_n & -\beta_n k \\ -2\alpha_n \mu_n k \gamma_n & -\beta_n \mu_n (k^2 + \nu_n^2) & 2\alpha_n \mu_n k \gamma_n & \beta_n \mu_n (k^2 + \nu_n^2) \\ -\alpha_n \mu_n (k^2 + \nu_n) & -2\beta_n \mu_n k \nu_n & -\alpha_n \mu_n (k^2 + \nu_n) & -2\beta_n \mu_n k \nu_n \end{pmatrix} \ . \tag{20}$$

Here $\gamma_n = \sqrt{k^2 - \omega/\alpha_n^2}$, $\nu_n = \sqrt{k^2 - \omega/\beta_n^2}$, k is the wavenumber, and μ_n, α_n, β_n are the shear modulus, P- and S-wave velocities of the n-th layer, respectively. $\hat{\mathbf{C}}_n$ is chosen as:

$$\hat{\mathbf{C}}_n = \begin{pmatrix} 1 & 0 \\ 0 & 1 \\ 0 & 0 \\ 0 & 0 \end{pmatrix} \ . \tag{21}$$

The displacement-stress vector bases are then computed at the half-space interface as:

$$\hat{\mathbf{C}}_{n-1} = \mathbf{L}_{n-1} \hat{\mathbf{Y}}_n \ . \tag{22}$$

Afterwards, $\hat{\mathbf{C}}_{n-1}$ is transformed by a 2×2 orthonormalization matrix $\mathbf{Q}$:

$$\hat{\mathbf{C}}'_{n-1} = \hat{\mathbf{C}}_{n-1} \mathbf{Q}_{n-1} \ , \tag{23}$$

with $\mathbf{Q}_{n-1}$ defined in such a way that elements $\hat{\mathbf{C}}'_{n-1,12}$ and $\hat{\mathbf{C}}'_{n-1,21}$ are zero:

$$\mathbf{Q}_{n-1} = \begin{pmatrix} \hat{\mathbf{C}}_{n-1,22} & -\hat{\mathbf{C}}_{n-1,22} \\ -\hat{\mathbf{C}}_{n-1,21} & \hat{\mathbf{C}}_{n-1,11} \end{pmatrix} / \sqrt{|\hat{\mathbf{C}}^{(1)}_{n-1}||\hat{\mathbf{C}}^{(2)}_{n-1}|} \ , \tag{24}$$

thus eliminating the operations between the growing exponential terms in the next step, in which the vector bases are propagated to the next interface:

$$\hat{\mathbf{Y}}_{n-1} = \mathbf{L}_{n-1} \mathbf{E}_{n-1} \hat{\mathbf{C}}'_{n-1} \tag{25}$$

where $\mathbf{E}_{n-1}$ is the 4×4 diagonal matrix (Aki & Richards, 2002):

$$\mathbf{E}_{n-1} = \begin{pmatrix} e^{\gamma_{n-1} d_{n-1}} & 0 & 0 & 0 \\ 0 & e^{\nu_{n-1} d_{n-1}} & 0 & 0 \\ 0 & 0 & e^{-\gamma_{n-1} d_{n-1}} & 0 \\ 0 & 0 & 0 & e^{-\nu_{n-1} d_{n-1}} \end{pmatrix} \ , \tag{26}$$

with d_{n-1} being the layer thickness. equation (19) to equation (25) are then solved iteratively upwards from the half-space interface until reaching the free surface ($n = 1$), where the boundary conditions for surface waves require the stress components to vanish. The dispersion curves can then be obtained by finding the pair of values (c, ω) that fulfill the equation (Aki & Richards, 2002):

$$\begin{vmatrix} \mathbf{Y}_{1,31} & \mathbf{Y}_{1,32} \\ \mathbf{Y}_{1,41} & \mathbf{Y}_{1,42} \end{vmatrix} = 0 \ . \tag{27}$$

However, this equation involves complex quantities due to the orthonormalization scheme, thus requiring a complicated root-finding procedure. In order to avoid this issue and deal with real quantities only, we adopt the approach of García-Jerez et al. (2016) and evaluate instead the signs of the following equation:

$$\begin{vmatrix} \mathbf{Y}_{1,31} & \mathbf{Y}_{1,32} \\ \mathbf{Y}_{1,41} & \mathbf{Y}_{1,42} \end{vmatrix} |\mathbf{Q}^*_{n-1}||\mathbf{Q}^*_{n-2}|...|\mathbf{Q}^*_1| = 0 \ , \tag{28}$$

The dispersion curves c_{R_m} for the fundamental and higher modes determined by evaluating equation (28) are combined together to form the apparent dispersion curve $c_R^{app}(\omega)$ as (Tokimatsu et al., 1992; Ohori et al., 2002):

$$\cos\left(\frac{\omega D}{c_R^{app}(\omega)}\right) \sum_{m=0}^{M} A^2_{R_m}(\omega) c_{R_m}(\omega) = \sum_{m=0}^{M} A^2_{R_m}(\omega) c_{R_m}(\omega) \cos\left(\frac{\omega D}{c_{R_m}(\omega)}\right) \ , \tag{29}$$

where $c_{R_m}(\omega)$ and $A_{R_m}(\omega)$ are the dispersion curve and the medium response function (Harkrider, 1964) associated with the m-th Rayleigh wave mode. Ohori et al. (2002) set D as the smallest inter-station distance in their array. In our approach, we set D as the minimum distance between the nodes of the grid used in the travel-time tomography.

The Rayleigh medium response function for the m-th mode takes the form (Harkrider & Anderson, 1966; Ben-Menahem & Singh, 2000):

$$A_{R_m}(\omega) = \frac{|u_{z_m}(\omega, z_1)|^2}{2U_{R_m}(\omega) c_R(\omega) I^R_{0_m}(\omega)} \ , \tag{30}$$

where $u_z(z_1)$ is the vertical displacement at the free surface, U_{R_m} is the m-th mode Rayleigh wave group velocity and $I^R_{0_m}$ is the energy integral given by (Harkrider & Anderson, 1966):

$$I^R_{0_m}(\omega) = \int_{\infty}^{0} \rho(z)(|u_{x_m}(\omega, z)|^2 + |u_{z_m}(\omega, z)|^2)dz \ . \tag{31}$$

In order to avoid computing numerical derivatives of the phase velocities, the group velocity can also be computed using energy integrals (García-Jerez et al., 2016):

$$U_{R_m}(\omega) = \frac{c_{R_m}(\omega)^2 I^R_{0_m}(\omega) - c_{R_m}(\omega)^2 I^R_{3_m}(\omega)/\omega^2 + I^R_{1_m}(\omega)}{2I^R_{0_m}(\omega)c_{R_m}(\omega)} \ , \tag{32}$$

with $I^R_{1_m}$ and $I^R_{3_m}$ being (Ben-Menahem & Singh, 2000; García-Jerez et al., 2016):

$$I^R_{1_m}(\omega) = \int_{\infty}^{0} \mu(z)(\frac{\alpha(z)^2}{\beta(z)^2}|u_{x_m}(\omega, z)|^2 + |u_{z_m}(\omega, z)|^2)dz \ , \text{ and} \tag{33}$$

$$I^R_{3_m}(\omega) = \int_{\infty}^{0} \mu(z)(\frac{\alpha(z)^2}{\beta(z)^2}\left|\frac{du_{z_m}(\omega, z)}{dz}\right|^2 + \left|\frac{du_{x_m}(\omega, z)}{dz}\right|^2)dz \ . \tag{34}$$

The vertical and horizontal Rayleigh wave displacements $u_{z_m}(\omega, z)$ and $u_{z_m}(\omega, z)$ needed for the computation of the energy integrals are the elements $\mathbf{r}_{R_m}(z)_{11}$ and $\mathbf{r}_{R_m}(z)_{12}$ of the displacement-stress vector $\mathbf{r}_{R_m}(z)$, which, following García-Jerez et al. (2016), can be computed for the j-th layer as:

$$\mathbf{r}_{R_m}(z) = \mathbf{L}_j\mathbf{E}_j(z - z_{j+1})\hat{\mathbf{C}}_j\mathbf{Q}_j\mathbf{Q}_{j-1}...\mathbf{Q}_1 \begin{pmatrix} \frac{-\mathbf{Y}_{1,32}}{\mathbf{Y}_{1,31}} \\ 1 \end{pmatrix} \ , \tag{35}$$

with $z_j \leq z \leq z_{j+1}$. As an example, Figure S1 shows the results of the forward modeling (dispersion curves for the fundamental mode and first three overtones, their corresponding medium-response functions, and the resulting apparent dispersion curve) for two synthetic models. The first of these models has two strong velocity inversions, which are reflected in two maxima in the medium response functions at approximately 0.1 and 0.2 Hz. In the second model, shear-wave velocity increases monotonically with depth and the corre-

sponding medium response functions for the higher modes are simpler, with the apparent dispersion curve being practically equal to that of the fundamental mode.

Text S5

Derivation of 1D shear-wave velocity models from the "exhumed mantle model"

In recent years, a new model for the structure of the Basque-Cantabrian Zone has been proposed, in which the mantle, uplifted during the Mesozoic, remained at < 10 km depth after the Pyrenean orogenesis, just beneath the sediments of the eastern Basque-Cantabrian Zone (Pedrera et al., 2017; García-Senz et al., 2019). The original gravity model by Pedrera et al. (2017) shows a large, rounded, piece of mantle beneath the Biscay synclinorium (see Figure 1 in the main text), in the Basque-Cantabrian Zone, from 5 to 30-32 km depth. In their model, this piece of mantle has a uniform density of 2.9 gr/cm^3, while the mantle below that depth has a density of 3.3 g/cm^3. In a reply to a comment by Pedreira et al. (2018), Pedrera et al. (2018) explain that the density of 2.9 g/cm^3 was due to mantle serpentinization and include a 2D magnetic model across the area (Gernika section), in which the exhumed mantle shows different values of magnetic susceptibility as a consequence of different degrees of serpentinization. A slight variation of this magnetic model, also including the fitting of gravity anomalies, was proposed later by García-Senz et al. (2019). In both cases, the average densities that can be inferred from the reported magnetic susceptibilities are much higher that the values used in their gravity models. Therefore, we derived two 1D shear-wave velocity profiles to test the "exhumed mantle model": one from the magnetic susceptibilities (serpentinization degree), and the other derived from the densities of the mantle.

In the closest point of the Gernika section to node 1575 (which lies 30 km to the ESE, approximately along the trace of the Biscay synclinorium; see Figure 2 in the main text), the magnetic model shows, from top to bottom: 7 km of Mesozoic-Cenozoic sedimentary and volcanic rocks, the Moho, 2-3 km of highly serpentinized peridotites with a magnetic susceptibility of 0.12 SI, 10 km of poorly serpentinized peridotites with a magnetic susceptibility of 0.0012 SI (Pedrera et al., 2018) or 0.004 SI (García-Senz et al., 2019), and a peridotite with a magnetic susceptibility of 0 SI. These susceptibilities can be broadly associated to average degrees of serpentinization of >75%, <25% and 0%, respectively (Oufi et al., 2002; Maffione et al., 2014). We assumed average values of 85%, 10% and 0% for those 3 mantle layers, from which we calculated the P-wave and S-wave velocities at 200 MPa and 200 °C for the uppermost segment (following Christensen, 2004), at 1 GPa and 400 °C for the deepest one (following Carlson & Miller, 2003), and an average between these two conditions for the intermediate segment (Table S1). These serpentinization values imply average densities of 2.58, 3.25 and 3.34 g/cm^3 at those conditions (Carlson & Miller, 2003; Christensen, 2004). Considering that the uppermost layer of 2.58 g/cm^3 is only 2-3 km thick, the volumetric average is clearly much higher than the 2.9 g/cm^3 reported by Pedrera et al. (2017) in their gravity model. We have added an extra mantle layer below 30 km depth with the same properties of the layer on top of it (i.e., no serpentinization) to give more freedom to the nonlinear inversion algorithm to fit the observed phase velocities. On top of the mantle, we included two layers of sediments with the same S-wave velocities of our initial model of Table 1 in the main text.

We can also estimate the V_s of the mantle from the density values used in the gravity models of the Gernika section. We find unrealistic to assume a constant density of 2.9

g/cm^3 as in the model of Pedrera et al. (2017), so we used instead the values proposed by (García-Senz et al., 2019). These authors consider a density of 2.7 g/cm^3 for the upper 2-3 km of highly serpentinized (>75%) exhumed mantle, and a variable density of 2.80-3.10 g/cm^3 for the remaining part of the mantle above 30-32 km depth, including the magnetized upper part (0.004 SI) and the fresh peridotites of the lower part (no susceptibility). Fresh peridotites below 30-32 km depth, on the other hand, have a density of 3.3 g/cm^3 in their model. From these densities, we calculated the Vs velocities again in the same way than in the previous case, following Carlson and Miller (2003) and Christensen (2004) (Table S2).

Text S6

Directionality of the seismic noise wavefield in the Basque-Cantabrian Zone

Since the azimuthal variations in the intensity of the seismic noise might have a small effect (in the order of 1-2%; Froment et al, 2010) on the measured velocities of surface waves, it is interesting to analyze the distribution of noise sources. Therefore, we performed a f-k analysis centered on the primary microseismic peak frequency following the approach described in Gal et al. (2014; their code is available at github.com/mgalcode/IAS-Capon). Since our network was deployed with the purpose of monitoring the local seismicity, it is ill-designed for the application of array techniques such as the f-k analysis, having an aperture of more than 400 km and an average interstation distance of 30 km. Instead, we have used a subset of 13 stations deployed in the Navarra area (green triangles in Figure 2 in the main text, excluding the easternmost one), which has a more reasonable aperture and average interstation distances of 70 and 10 km, respectively. The results of the f-k analysis are presented in Figure S4 and show that the most intense seismic noise sources

are located to the north of the study area, while a sufficient level of noise arises from all azimuthal sectors.

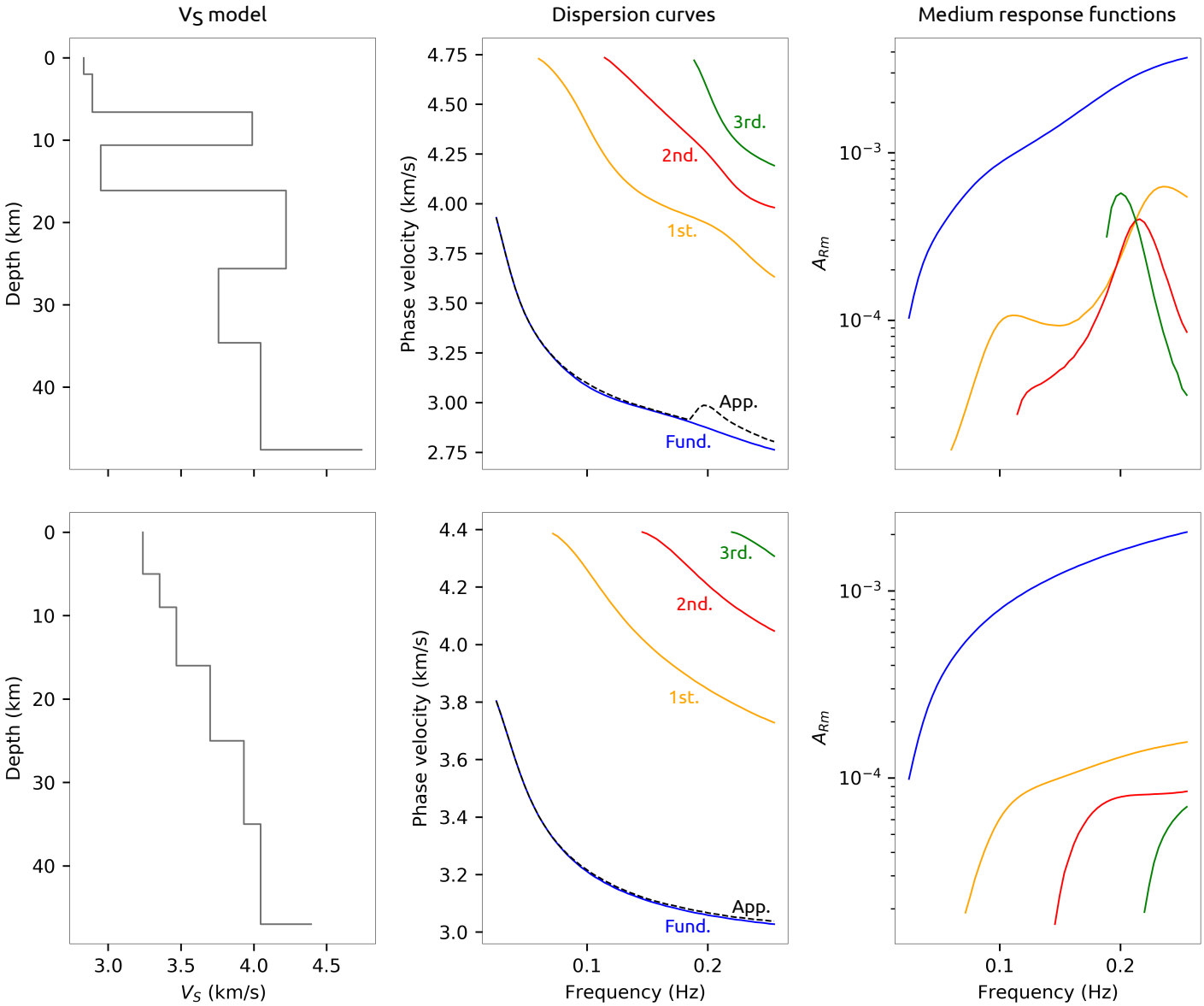

Figure S1. Rayleigh wave dispersion curves for the fundamental mode (Fund.) and higher modes (1st, 2nd and 3rd) and their corresponding medium response functions computed for two synthetic models: one with two strong velocity inversions (top row) and another with monotonically increasing shear-wave velocities (bottom row). The apparent dispersion curve for each model is shown as a dashed black line labeled as "App.".

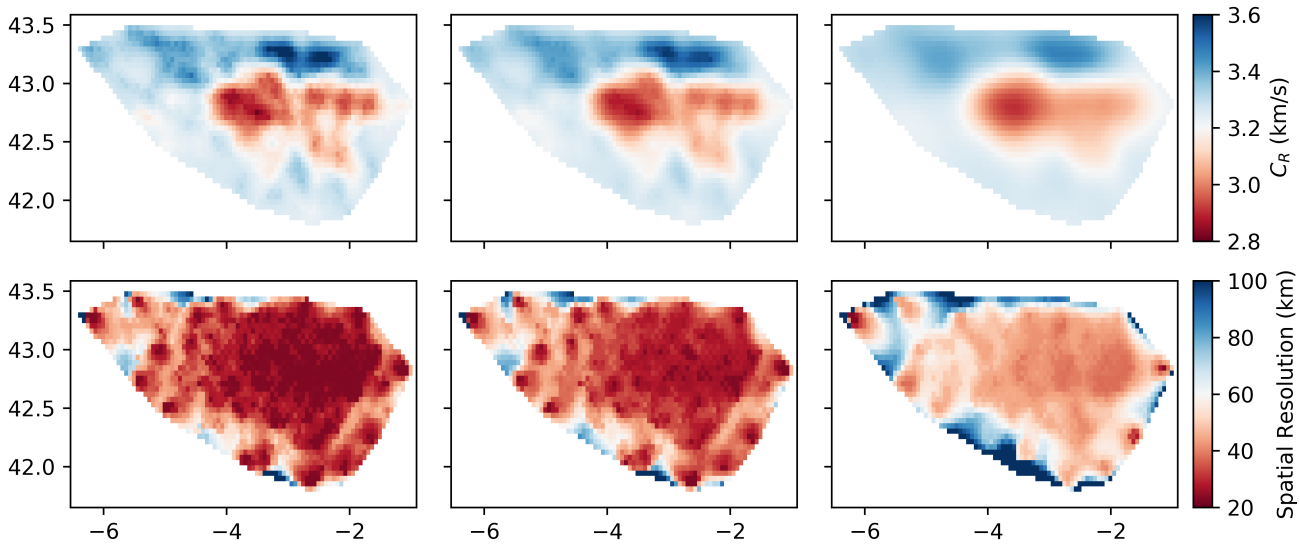

Figure S2. Comparative of the results of the travel-time linearized inversion for a period of 14 s, using a smoothing parameter of 40 (left), 400 (middle) and 4000 (right). For smoothing values of 40 and 400, the positions of some stations and a few interstation paths can be seen (artifacts), which suggests that the choice of parameters is not adequate. In this case, the map on the right is clearly preferable since the spatial resolution values shown below are reasonable given an average wavelength of 45 km.

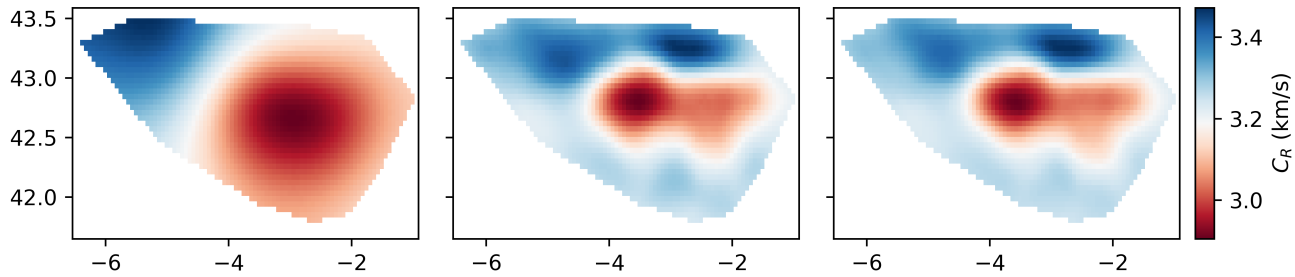

Figure S3. Comparative between the results of the travel-time linearized inversion for a period of 14 s with and without the outlier removal step (left) Result from the overdamped inversion performed in the first step of the linearized inversion, (middle) result of the inversion without removing outliers, (right) result of the inversion after outliers removal. The smoothing parameter used in the first step is 10 times the one used in the final inversion (40000 and 4000, respectively).

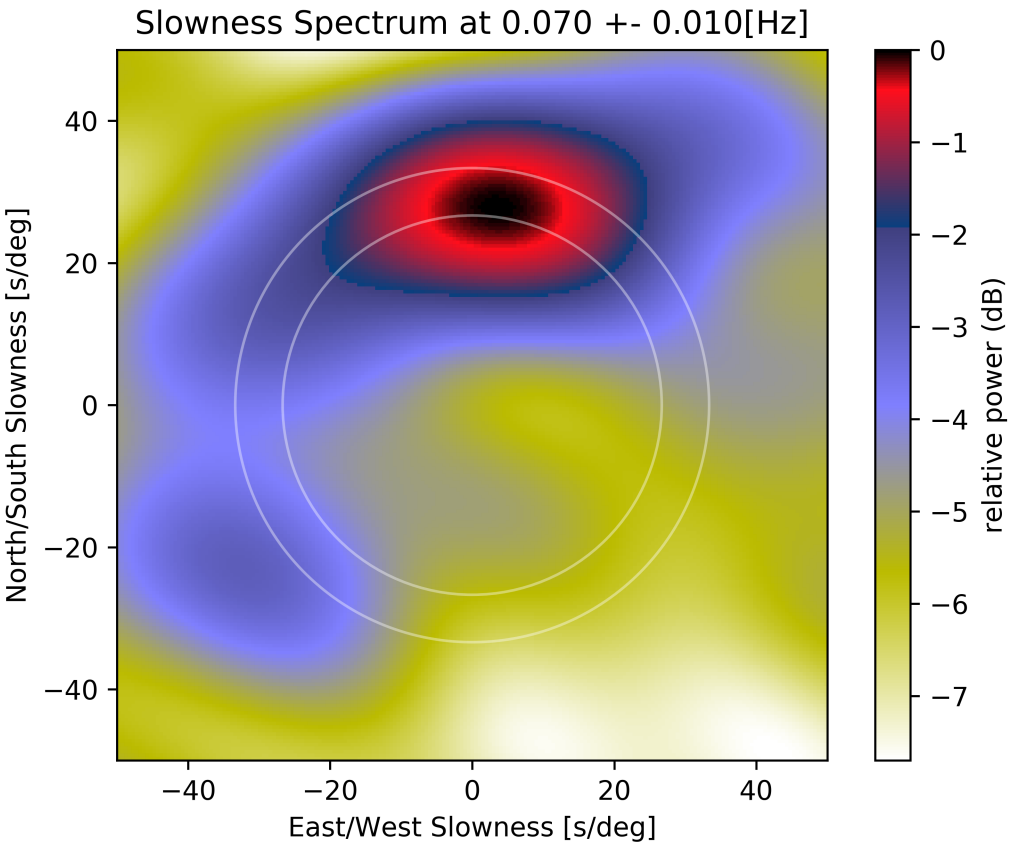

Figure S4. Results of the f-k analysis centered in the primary microseismic peak frequency using a subset of 13 stations located in the Navarra area.

Layer	Thickness (km)	Vp (km/s)	Vs (km/s)	Inferred densities for the mantle (g/cm^3)
Mesozoic-Cenozoic (top)	3	4.80	2.77	
Mesozoic-Cenozoic (bottom)	4	5.00	2.89	
Mantle, ∼85% serpentinized	3	5.30	2.60	2.58
Mantle, ∼10% serpentinized	10	7.72	4.18	3.25
Mantle, 0% serpentinized	10	8.10	4.30	3.34
Mantle, 0% serpentinized	20	8.10	4.30	3.34

Table S1. 1D body-wave velocity model based on the "exhumed mantle model" by Pedrera et al. (2017, 2018) and García-Senz et al. (2019), with Vp and Vs of the mantle layers derived from their magnetic susceptibilities ("magnetic model"). See Text S5 for details.

Layer	Thickness (km)	Density (g/cm^3)	Vp (km/s)	Vs (km/s)
Mesozoic-Cenozoic (top)	3	2.60	4.80	2.77
Mesozoic-Cenozoic (bottom)	4	2.67	5.00	2.89
Mantle, >75% serpentinized	3	2.70	5.70	2.91
Mantle, ∼10% serpentinized	10	2.80	6.03	2.98
Mantle, 0% serpentinized	10	3.10	7.30	3.75
Mantle, 0% serpentinized	20	3.30	8.10	4.30

Table S2. 1D body-wave velocity model based on the "exhumed mantle model", with Vp and Vs of the mantle derived from their densities (gravity model of García-Senz et al., 2019). See Text S5 for details

References

Aki, K. (1957). Space and time spectra of stationary stochastic waves, with special reference to microtremors. *Bulletin of the Earthquake Research Institute*, *35*, 415-456.

Aki, K., & Richards, P. G. (2002). *Quantitative Seismology* (2nd ed.). University Science Books, Sausalito, California.

Barmin, M. P., Ritzwoller, M. H., & Levshin, A. L. (2001). A fast and reliable method for surface wave tomography. *Pure and Applied Geophysics*, *158*, 1351-1375. doi: 10.1007/PL00001225

Ben-Menahem, A., & Singh, S. J. (2000). *Seismic waves and sources.* Springer, New York, NY. doi: 10.1007/978-1-4612-5856-8

Carlson, R. L., & Miller, D. J. (2003). Mantle wedge water contents estimated from seismic velocities in partially serpentinized peridotites. *Geophysical Research Letters*, *30 (5)*. doi: 10.1029/2002GL016600

Christensen, N. I. (2004). Serpentinites, Peridotites, and Seismology. *International Geology Review*, *46*. doi: 10.2747/0020-6814.46.9.795

Ekström, G. (2014). Love and Rayleigh phase velocity maps, 5-40 s, of the western and central usa from usarray data. *Earth and Planetary Science Letters*, *402*, 42-49. doi: 10.1016/j.epsl.2013.11.022

García-Jerez, A., Piña-Flores, J., Sánchez-Sesma, F. J., Luzón, F., & Perton, M. (2016). A computer code for forward calculation and inversion of the H/V spectral ratio under the diffuse field assumption. *Computers & Geosciences*, *97*, 67-78. doi: 10.1016/j.cageo.2016.06.016

García-Senz, J., Pedrera, A., Ayala, C., Ruiz-Constán, A., Robador, A., & Rodríguez-Fernández, L. R. (2019). Inversion of the north Iberian hyperextended margin: the role of exhumed

mantle indentation during continental collision. *Tectonics*, *36 (12)*, 3155-3177. doi: 10.1002/2017TC004716

Goutorbe, B., Oliveira Coelho, D. L., & Drouet, S. (2015). Rayleigh wave group velocities at periods of 6-23 s across Brazil from ambient noise tomography. *Geophysical Journal International*, *203*, 869-882. doi: 10.1093/gji/ggv343

Harkrider, D. G. (1964). Surface waves in multilayered elastic media I. Rayleigh and Love waves from buried sources in a multilayered elastic half-space. *Bulletin of the Seismological Society of America*, *54(2)*, 627-679.

Harkrider, D. G., & Anderson, D. L. (1966). Surface wave energy from point sources in plane layered Earth models. *Journal of Geophysical Research*, *71(12)*, 2967-2980. doi: 10.1029/JZ071i012p02967

Haskell, N. A. (1953). The dispersion of surface waves on multilayered media. *Bulletin of the Seismological Society of America*, *43(1)*, 17-34.

Maffione, M., Morris, A., Plümper, O., & van Hinsbergen, D. J. J. (2014). Magnetic properties of variably serpentinized peridotites and their implication for the evolution of oceanic core complexes. *Geochemistry, Geophysics, Geosystems*, *15*, 923-944. doi: 10.1002/2013GC004993

Menke, W., & Jin, G. (2015). Waveform fitting of cross spectra to determine phase velocity using Aki's formula. *Bulletin of the Seismological Society of America*, *105*, 1619-1627. doi: 10.1785/0120140245

Ohori, M., Nobata, A., & Wakamatsu, K. (2002). A comparison of ESAC and FK methods of estimating phase velocity using arbitrarily shaped microtremor arrays. *Bulletin of the Seismological Society of America*, *92*, 2323-2332. doi: 10.1785/0119980109

Oufi, O., Cannat, M., & Horen, H. (2002). Magnetic properties of variably serpentinized abyssal

peridotites. *Journal of Geophysical Research - Solid Earth*, *107 (B5)*, EPM 3-1-EPM 3-19. doi: 10.1029/2001JB000549

Pedreira, D., Pulgar, J. A., Díaz, J., Alonso, J. L., Gallastegui, J., & Teixell, A. (2018). Comment on "Reconstruction of the Exhumed Mantle Across the North Iberian Margin by Crustal-Scale 3-D Gravity Inversion and Geological Cross Section" by Pedrera et al. *Tectonics*, *37*, 4338-4345. doi: 10.1029/2018TC005129

Pedrera, A., García-Senz, J., Ayala, C., Ruiz-Constán, A., Rodríguez-Fernández, L. R., Robador, A., & González Menéndez, L. (2017). Reconstruction of the Exhumed Mantle Across the North Iberian Margin by Crustal-Scale 3-D Gravity Inversion and Geological Cross Section. *Tectonics*, *36 (12)*, 3155-3177. doi: 10.1002/2017TC004716

Pedrera, A., García-Senz, J., Ayala, C., Ruiz-Constán, A., Rodríguez-Fernández, L. R., Robador, A., & González Menéndez, L. (2018). Reply to Comment by Pedreira et al. on "Reconstruction of the Exhumed Mantle Across the North Iberian Margin by Crustal-Scale 3-D Gravity Inversion and Geological Cross Section". *Tectonics*, *37*. doi: 10.1029/2018TC005222

Pilz, M., Parolai, S., & Woith, H. (2017). A 3-D algorithm based on the combined inversion of Rayleigh and Love waves for imaging and monitoring of shallow structures. *Geophysical Journal International*, *209*, 152-166. doi: 10.1093/gji/ggx005

Prieto, G. A., Lawrence, J. F., & Beroza, G. C. (2009). Anelastic Earth structure from the coherency of the ambient seismic field. *Journal of Geophysical Research*, *114*, B07303. doi: 10.1029/2008JB006067

Schwab, F., & Knopoff, L. (1970). Surface wave dispersion computations. *Bulletin of the Seismological Society of America*, *60*, 321-344.

Tang, X. M., Li, C., & Patterson, D. J. (2010). A curve-fitting technique for determining dispersion characteristics of guided elastic waves. *Geophysics*, *75*, 153-160. doi: 10.1190/1.3420736

Tokimatsu, K., Tamura, S., & Kojima, H. (1992). Effects of multiple modes on Rayleigh wave dispersion characteristics. *Journal of Geotechnical Engineering*, *118(10)*, 1529-1543. doi: 10.1061/(ASCE)0733-9410(1992)118:10(1529)

Wang, R. (1999). A simple orthonormalization method for stable and efficient computation of green's functions. *Bulletin of the Seismological Society of America*, *89(3)*, 733-741.